

Laplace deconvolution on the basis of time domain data and its application to Dynamic Contrast Enhanced imaging

FABIENNE COMTE^{1,2}, CHARLES-A. CUENOD^{1,3}, MARIANNA PENSKEY⁴
and YVES ROZENHOLC^{1,2,5}

Université Paris Descartes¹, MAP5, UMR CNRS 8145², LRI INSERM U970 PARCC-HEGP³,
University of Central Florida⁴ and INRIA Saclay Ile-de-France SELECT⁵

Corresponding author: F. Comte, Université Paris Descartes, MAP5, UMR CNRS 8145, France
fabienne.comte@parisdescartes.fr

Abstract

In the present paper we consider the problem of Laplace deconvolution with noisy discrete non-equally spaced observations on a finite time interval. We propose a new method for Laplace deconvolution which is based on expansions of the convolution kernel, the unknown function and the observed signal over Laguerre functions basis (which acts as a surrogate eigenfunction basis of the Laplace convolution operator) using regression setting. The expansion results in a small system of linear equations with the matrix of the system being triangular and Toeplitz. Due to this triangular structure, there is a common number m of terms in the function expansions to control, which is realized via complexity penalty. The advantage of this methodology is that it leads to very fast computations, produces no boundary effects due to extension at zero and cut-off at T and provides an estimator with the risk within a logarithmic factor of m of the oracle risk. We emphasize that, in the present paper, we consider the true observational model with possibly non-equispaced observations which are available on a finite interval of length T which appears in many different contexts, and account for the bias associated with this model (which is not present in the case of $T \rightarrow \infty$).

The study is motivated by perfusion imaging using a short injection of contrast agent, a procedure which is applied for medical assessment of micro-circulation within tissues such as cancerous tumors. Presence of a tuning parameter a allows to choose the most advantageous time units, so that both the kernel and the unknown right hand side of the equation are well represented for the deconvolution. The methodology is illustrated by an extensive simulation study and a real data example which confirms that the proposed technique is fast, efficient, accurate, usable from a practical point of view and very competitive.

AMS 2010 subject classifications. 62G05, 62G20, 62P10.

Key words and phrases: Laplace deconvolution, Complexity penalty, Model selection, Dynamic Contrast Enhanced imaging, Perfusion imaging.

1 Introduction

Consider the Laplace convolution model

$$y(t_i) = \int_0^{t_i} g(t_i - \tau)f(\tau)d\tau + \sigma\varepsilon_i, \quad i = 1, \dots, n, \quad (1.1)$$

which is a discrete noisy version of the linear Volterra equation of the first kind

$$q(t) = \int_0^t g(t-\tau)f(\tau)d\tau = \int_0^t g(\tau)f(t-\tau)d\tau, \quad t \geq 0, \quad (1.2)$$

where function g is considered to be known, f is a function of interest, measurements $y(t_i)$ are taken at points $0 \leq t_1 \leq \dots \leq t_n \leq T < \infty$, and the errors ε_i are i.i.d. sub-Gaussian random variables with $\mathbb{E}\varepsilon_i = 0$ and $\text{Var}(\varepsilon_i) = 1$ (see Vershynin (2012) for definition and discussion of sub-Gaussian random variables).

The study is motivated by high frequency perfusion imaging such as Dynamical Contrast Enhanced (DCE) imaging using either Computerized Tomography (DCE-CT), Magnetic Resonance Imaging (DCE-MRI) or Ultra Sound (DCE-US). Those techniques have a great potential in cancer treatments but suffer from the lack of robust quantification as pointed out by Cao (2011). Model (1.1) is also used for describing time-resolved measurements in fluorescence spectroscopy (see, e.g. Ameloot and Hendrickx (1983), Ameloot *et al.* (1984), Gafni *et al.* (1975), O'Connor *et al.* (1979) and also the monograph of Lakowicz (2006) and references therein).

We solve the problem (1.1) in a non-asymptotic setting where both n and T are not large, and time instances are not equally spaced, corresponding to the medical set-up which necessarily controls the patient's exposure to radiation together with the duration of the whole exam and is limited by the acquisition technique. Our objective is to design a technique which performs well under those conditions in a sense that it has minimal or nearly minimal possible error and can be used when function g is only partially observed. Therefore, we do not replace equation (1.1) by an "ideal" white noise model which immensely simplifies the issues and carry out error analysis in a practical observational set up. Below, we discuss existing methodologies and their limitations.

Solution by the Laplace transform

The mathematical theory of (noiseless) convolution type Volterra equations is well developed (see, e.g., Gripenberg *et al.* 1990) and the exact solution of equation (1.2) can be obtained through Laplace transform. However, direct application of Laplace transform for discrete measurements faces serious conceptual and numerical problems. The inverse Laplace transform is usually found by application of tables of inverse Laplace transforms, partial fraction decomposition or series expansion (see, e.g., Polyanin and Manzhirov, 1998), neither of which is applicable in the case of the discrete noisy version of Laplace deconvolution.

Numerical inversion of Laplace transform becomes unstable due to requirement of dividing it by the Laplace transform of function g . Although the recently proposed maximum entropy method of Mnatsakanov (2011) and Mnatsakanov and Sarkisian (2013) works well for large sample sizes ($n \geq 500$), it dramatically deteriorates in the situations where n is small and one needs to recover solution of an ill-posed problem.

Fourier deconvolution

Formally, by setting $g(t) = f(t) \equiv 0$ for $t < 0$, equation (1.2) can be viewed as a particular case of the Fourier convolution equation

$$q(t) = \int_{-\infty}^{\infty} g(t-\tau)f(\tau)d\tau. \quad (1.3)$$

Discrete stochastic version of equation (1.3)

$$y(t_i) = \int_a^b g(t_i - \tau)f(\tau)d\tau + \sigma\varepsilon_i, \quad i = 1, \dots, n, \quad (1.4)$$

known also as Fourier deconvolution problem, has been extensively studied in the last thirty years (see, for example, Carroll and Hall, 1988; Comte, Rozenholc and Taupin, 2006; Delaigle, Hall and Meister, 2008; Diggle and Hall, 1993; Fan, 1991; Fan and Koo, 2002; Johnstone *et al.*, 2004; Pensky and Vidakovic, 1999; Stefanski and Carroll, 1990, among others).

However, such an approach is very misleading. To start with, although in (1.2) one has $0 \leq t \leq T$ with $T < \infty$, equation $q(t) = \int_0^T g(t-\tau)f(\tau)d\tau$ **is not** a Fourier convolution equation on the interval $[0, T]$, in the sense that application of the Fourier transform on an interval $[0, T]$ **does not** convert the integral into a product of the Fourier transforms of f and g unless these functions g and f are periodic on $[0, T]$, which is very unlikely to happen in applications. Therefore, one has to apply the Fourier transform on the real line to equation (1.3). This application faces multiple obstacles: for small values of n and T , inverse Fourier transform has poor precision since Fourier transform inherently operates on the whole real line and requires integration of highly oscillatory functions. In addition, the true solution $f(\tau)$ may not vanish at $\tau = 0$, which introduces an additional instability into the Fourier transform solution, due to a jump discontinuity of f at zero. Those difficulties, however, are not intrinsic to the problem and are entirely due to the usage of Fourier transform. Indeed, the concern of having measurements only for $t \leq T$ does not affect the Laplace deconvolution since it exhibits **causality** property: the values of $q(t)$ for $0 \leq t \leq T$ depend on values of $f(t)$ for $0 \leq t \leq T$ only and vice versa. Moreover, since function f is considered only for $t \geq 0$, the issue of its discontinuity at zero does not arise.

Mathematical approaches

Several scientists attempted to solve equation (1.1) using discretization and then applying standard methodologies like the singular value decomposition (SVD) and the Tikhonov regularization (see, e.g., Lamm (1996), Cinzori and Lamm (2000), and, in the context of perfusion imaging, Ostergaard *et al.* (1996) and an extensive review in Fieselmann *et al.* (2011)). The shortcoming of these methods is that they are designed for a general linear inverse problem and do not take advantage of a particular form of the equation. In what follows, we compare our method with the SVD approach and confirm that the latter one delivers very inferior estimators. In particular, the estimators exhibit strong instabilities at $t = 0$.

Methodology of Ameloot and Hendrickx (1983) is designed specifically for analysis of fluorescence curves. It relies on parametric presentation of the solution f as a sum of exponential functions and requires the knowledge of the number of components. The approach is suitable only for the situation when the solution indeed has this parametric form and the number of components is small since the exponential functions are highly correlated.

The technique of Maleknejad *et al.* (2007) is based on the expansion of the solution over the Haar wavelet basis. The paper uses only the scaling parts of the Haar basis and finds coefficients by minimization of the discrepancy with the right-hand side. The authors assume the functions of interest to be piecewise constant and, hence, have an efficient representation in Haar wavelet basis, which is not the case in our particular application. Moreover, since the methodology is designed for exact measurements, the authors offer no tools for model selection and do not provide statistical error bounds. Hence, despite being a general solution of the Laplace deconvolution problem, this method is not a good option in the case of a small number of noisy irregularly spaced observations.

Statistical approaches

Unlike Fourier deconvolution, that has been intensively studied in statistical literature (see references above), Laplace deconvolution received very little attention within statistical framework. To the best of our knowledge, before 2010, only Dey, Martin and Ruymgaart (1998) tackled the statistical version of the problem. They considered a noisy version of Laplace deconvolution with a very specific kernel of the form $g(t) = be^{-at}$ and assumed that data are available on the whole positive half-line (i.e. $T = \infty$) and that smoothness of f is known (i.e., the estimator is not adaptive).

Abramovich *et al.* (2013) studied the problem of Laplace deconvolution based on discrete noisy data on a finite interval $[0, T]$. The idea of the method is to reduce the problem to estimation of the unknown regression function and its derivatives, using kernel method with an adaptive choice of the bandwidth. The method has an advantage of reducing the Laplace deconvolution problem to a well studied nonparametric regression problem. Nevertheless, the shortcoming of the technique is that it is strongly dependent on **the exact knowledge** of the kernel g on the positive real line since it relies on the analytic inversion of the equation. In particular, it requires the knowledge of the roots of the Laplace transform of the kernel g , leading to an extremely unstable estimator when exact analytic expression of the kernel is unknown and g is reconstructed using some measurements. Indeed, small change in the observations of g produces significant changes in the roots and, hence, in the expression of the estimator. In addition, technique of Abramovich *et al.* (2013) requires meticulous boundary correction.

Current methodology

The present paper offers a method which is designed to overcome limitations of the previously developed techniques. The new methodology allows one to use real-time data and is based on expansions of the kernel, unknown function f and the right-hand side in equation (1.1) over the Laguerre functions basis. As it was noticed before (see, e.g. Weeks (1966) or Lien *et al.* (2008)), the Laguerre functions basis provides a surrogate eigenfunction basis for the problem since the expansions result in a small system of linear equations with the matrix of the system being lower triangular and Toeplitz. The number of the terms in the expansion of the estimator is controlled via complexity penalty.

The technique does not require exact knowledge of the kernel since it is represented by its Laguerre coefficients only, so, unlike Abramovich *et al.* (2013), it can be easily applied in the case when the kernel g is not known exactly but is estimated from observations. The recent Vareschi (2015) paper, which is built upon the first initial version of our manuscript (Comte *et al.* (2012)), makes this extension. However, Vareschi (2015) considers a purely theoretical version of the model where one samples Laguerre coefficients directly. Contrary to this, in the present version of the paper, we provide a true solution to the initial problem (1.1) and estimate Laguerre coefficients in the regression set up. Note that, since Laguerre coefficients depend on the values of a function on $(0, \infty)$, estimation of the coefficients on the basis of limited data leads to an additional bias term which can be made smaller than the squared bias and the variance of the penalized estimator. We provide an oracle inequality for the risk of the estimator and prove that, under mild assumptions on the model, the estimator is nearly optimal with the risk within $\log n$ factor of the minimal risk.

We would like to emphasize that, in the present paper, we examine the true observational model, where measurements are available only on a finite interval of length T and are possibly non-equispaced. This is a suitable description of data involved in, e.g. high frequency perfusion imaging as well as in other applications such as fluorescent spectroscopy. To the best of our knowledge, so far this careful consideration has never been carried out and can be reproduced in many contexts where

one needs to use coefficient-based model when only finite number of non-equispaced observations are available.

Since our construction is based on application of Laguerre functions and the inversion of a triangular system, it leads to very fast computations and produces no boundary effects that are due to the extension at zero and cut-off at T . The presence of a tuning parameter a allows for the choice of the most advantageous time units, so that both the kernel and the unknown right hand side of the equation are efficiently represented for the further deconvolution.

The methodology is illustrated by an extensive simulation study using both earlier examples studied in Abramovich *et al.* (2013) and new settings based on the kernels g observed in the real DCE experiments. Simulation study confirms that the proposed technique is fast, efficient, accurate, practically usable and highly competitive: the new methodology easily outperforms the SVD, the Tikhonov regularization and the kernel-based technique of Abramovich *et al.* (2013). The software is available on request for non-profit research purposes from Dr. Yves Rozenholc (yves.rozenholc@parisdescartes.fr).

The rest of the paper is organized as follows. In Section 2 we derive a system of equations resulting from expansion of the functions over the Laguerre basis, study the effect of discrete, possible irregularly spaced data and introduce selection of model size via penalization. Corollary 1 indeed confirms that the risk of the penalized estimator lies within a logarithmic factor of the minimal risk. In Section 3 we extend our study to the case $T \rightarrow \infty$ and provide asymptotic upper bounds for the risk proving that the risk lies within a logarithmic factor of an oracle risk. The proof of this fact rests on nontrivial facts of the theory of Toeplitz matrices. Section 4 considers high frequency perfusion imaging as an important motivating example for the theoretical investigations of the paper. Section 5 provides an extensive simulation study. Section 6 presents an example of application of the methodology developed in the paper to analysis of a DCE-MRI sequence of images of a participant of the REMISCAN cohort study [40] who underwent anti-angiogenic treatment for renal cancer. Finally, Section 7 concludes the paper with discussion of results. Section 8 contains some essential proofs. The rest of the proofs and other supplementary materials such as introduction to theory of banded Toeplitz matrices and some of simulation results can be found in Section A, Appendix.

2 Laplace deconvolution via expansion over Laguerre functions basis

2.1 Notations

In what follows, we use letters f , g and q for functions $f(x)$, $g(x)$ and $q(x)$, respectively. Vectors of values of those functions at points t_1, \dots, t_n are denoted by \vec{f} , \vec{g} and \vec{q} . Vectors of Laguerre coefficients are denoted by bold letters (e.g. $\mathbf{f}_m, \mathbf{g}_m, \mathbf{q}_m$) with the subscript indicating dimension of the vector. The coordinates of these vectors are denoted with using superscripts: $\mathbf{f}_m = (f^{(0)}, \dots, f^{(m-1)})^T$, where u^T denotes the transpose of u .

Given a matrix \mathbf{A} , let \mathbf{A}^T be the transpose of \mathbf{A} , $\|\mathbf{A}\|_2^2 = \text{Tr}(\mathbf{A}^T \mathbf{A})$ and $\rho^2(\mathbf{A}) = \lambda_{\max}(\mathbf{A}^T \mathbf{A}) = \lambda_{\max}(\mathbf{A} \mathbf{A}^T)$ be, respectively, the Frobenius and the spectral norm of a matrix \mathbf{A} , where $\lambda_{\max}(\mathbf{U})$ is the largest, in absolute value, eigenvalue of \mathbf{U} . We denote by $[\mathbf{A}]_m$ the upper left $m \times m$ sub-matrix of \mathbf{A} . Given a vector $u \in \mathbb{R}^k$, we denote by $\|u\|$ its Euclidean norm and, for $p \leq k$, the $p \times 1$ vector with the first p coordinates of u , by $[u]_p$. For any function $t \in L_2(\mathbb{R}_+)$, we denote by $\|t\|_2$ its L_2 norm on \mathbb{R}_+ .

2.2 Coefficients of the Laguerre expansion and their estimators

In what follows, we assume that f is square integrable over the positive half line \mathbb{R}^+ . Then, a common solution to the problem (1.1) is to represent f , g , q and y in equations (1.1) and (1.2) via some orthonormal basis on \mathbb{R}^+ , thus, reducing (1.1) and (1.2) to a linear system of equations. It turns out that the Laguerre functions

$$\phi_k(t) = \sqrt{2a}e^{-at}L_k(2at), \quad k = 0, 1, \dots, \quad (2.1)$$

where $L_k(t)$ are Laguerre polynomials (see, e.g., Gradshteyn and Ryzhik (1980))

$$L_k(t) = \sum_{j=0}^k (-1)^j \binom{k}{j} \frac{t^j}{j!}, \quad t \geq 0,$$

form a basis, which is particularly suitable for the problem at hand since it acts as a surrogate eigenfunction basis for the problem (see, e.g. Weeks (1966) or Lien *et al.* (2008)). Traditionally, one uses $a = 1/2$, however, introduction of an additional parameter a allows to choose the most appropriate time scale in the real-life applications of the methodology in general, and to perfusion imaging that motivates our study, in particular.

We denote by $f^{(k)}$, $g^{(k)}$, $q^{(k)}$ and $y^{(k)}$, $k = 0, \dots, \infty$, the coefficients of the expansions over the Laguerre function basis of the functions $f(\cdot)$, $g(\cdot)$, $q(\cdot)$ and $y(\cdot)$ respectively. By plugging these expansions into formula (1.2), we obtain the following equation

$$\sum_{k=0}^{\infty} q^{(k)} \phi_k(t) = \sum_{k=0}^{\infty} \sum_{j=0}^{\infty} f^{(k)} g^{(j)} \int_0^t \phi_k(x) \phi_j(t-x) dx. \quad (2.2)$$

Due to the following relation (see, e.g., 7.411.4 in Gradshteyn and Ryzhik (1980))

$$\int_0^t \phi_k(x) \phi_j(t-x) dx = 2ae^{-at} \int_0^t L_k(2ax) L_j(2a(t-x)) dx = (2a)^{-1/2} [\phi_{k+j}(t) - \phi_{k+j+1}(t)],$$

equation (2.2) can be re-written as

$$\sum_{k=0}^{\infty} q^{(k)} \phi_k(t) = \sum_{k=0}^{\infty} \phi_k(t) [(2a)^{-1/2} f^{(k)} g^{(0)} + \sum_{\ell=0}^{k-1} (2a)^{-1/2} (g^{(k-\ell)} - g^{(k-\ell-1)}) f^{(\ell)}].$$

Equating coefficients for each of the basis functions, we obtain an infinite triangular system of linear equations. In order to use this system for estimating f , we denote the approximation of f based on the first m Laguerre functions by

$$f_m(x) = \sum_{k=0}^{m-1} f^{(k)} \phi_k(x). \quad (2.3)$$

The following Lemma states how the coefficients in (2.3) can be recovered.

Lemma 1. *Let \mathbf{f}_m and \mathbf{q}_m be m -dimensional vectors with elements $f^{(k)}$ and $q^{(k)}$, $k = 0, 1, \dots, m-1$, respectively. Then, for any m , one has $\mathbf{q}_m = \mathbf{G}_m \mathbf{f}_m$ where \mathbf{G}_m is the lower triangular Toeplitz matrix with the first column $(g^{(0)}, g^{(1)} - g^{(0)}, \dots, g^{(m-1)} - g^{(m-2)})^T / \sqrt{2a}$.*

Applying Lemma 1 for $1 \leq m \leq M$, we construct the following collection of estimators of $f(x)$

$$\hat{f}_m(x) = \sum_{k=0}^{m-1} \hat{f}^{(k)} \phi_k(x) \quad (2.4)$$

where $\widehat{\mathbf{f}}_m = (\hat{f}^{(0)}, \dots, \hat{f}^{(m-1)}) = [\widehat{\mathbf{f}}_M]_m$. Here, $\widehat{\mathbf{f}}_M = \mathbf{G}_M^{-1} \widehat{\mathbf{q}}_M$ and

$$\widehat{\mathbf{q}}_M := (\Phi_M^T \Phi_M)^{-1} \Phi_M^T \vec{y} \quad (2.5)$$

is the unbiased estimator of $(\Phi_M^T \Phi_M)^{-1} \Phi_M^T \vec{q}$ with $\vec{q} := (q(t_1), \dots, q(t_n))^T$, $\vec{y} := (y(t_1), \dots, y(t_n))^T$ and

$$\Phi_M := \begin{pmatrix} \phi_0(t_1) & \dots & \phi_{M-1}(t_1) \\ \phi_0(t_2) & \dots & \phi_{M-1}(t_2) \\ \vdots & \dots & \vdots \\ \phi_0(t_n) & \dots & \phi_{M-1}(t_n) \end{pmatrix}.$$

Denoting $\mathbf{J}_{m,M} = (\mathbf{I}d_m \quad \mathbf{0}_{m,M-m})$ the $m \times M$ matrix which has the $m \times m$ identity matrix $\mathbf{I}d_m$ as its first m columns and the rest of the columns are equal to zero, the following relations hold

$$\widehat{\mathbf{f}}_m = [\widehat{\mathbf{f}}_M]_m = [\mathbf{G}_M^{-1} (\Phi_M^T \Phi_M)^{-1} \Phi_M^T \vec{y}]_m = \mathbf{G}_m^{-1} \mathbf{J}_{m,M} \widehat{\mathbf{q}}_M = \mathbf{G}_m^{-1} \mathbf{J}_{m,M} (\Phi_M^T \Phi_M)^{-1} \Phi_M^T \vec{y}. \quad (2.6)$$

Note that, by using estimator (2.6) instead of the seemingly intuitive estimator $\mathbf{G}_m^{-1} \widehat{\mathbf{q}}_m$, we manage to achieve two goals: avoiding re-fitting of the models for each value of m and reducing the bias that is due to having observations of the values of \vec{y} rather than the noisy versions of Laguerre coefficients.

In order to understand the nature of this additional bias, observe that equation (1.1) is equivalent to

$$\vec{y} = \Phi_\infty \mathbf{q}_\infty + \sigma \vec{\varepsilon} \quad (2.7)$$

where $\vec{\varepsilon} := (\varepsilon_1, \dots, \varepsilon_n)^T$ and Φ_∞ and \mathbf{q}_∞ are the infinite versions of Φ_M and \mathbf{q}_M . Consider vector $\vec{q}_M := (q_M(t_1), \dots, q_M(t_n))^T$, where $q_M(\cdot)$ is the orthogonal projection of q on the space spanned by the functions $\phi_0, \dots, \phi_{M-1}$. Then, $\vec{q}_M = \Phi_M \mathbf{q}_M$. Heuristically replacing $\Phi_\infty \mathbf{q}_\infty$ in (2.7) by $\Phi_M \mathbf{q}_M$ and following the construction of the linear regression estimator, we estimate \mathbf{q}_M by $\widehat{\mathbf{q}}_M = (\Phi_M^T \Phi_M)^{-1} \Phi_M^T \vec{y}$ as given by (2.5). Note that $\mathbf{q}_M = (\Phi_M^T \Phi_M)^{-1} \Phi_M^T \vec{q}_M$ but $\mathbb{E}(\widehat{\mathbf{q}}_M) = (\Phi_M^T \Phi_M)^{-1} \Phi_M^T \Phi_\infty \mathbf{q}_\infty$, so estimator $\widehat{\mathbf{q}}_M$ contains an additional bias $\mathbf{q}_M - \mathbb{E}(\widehat{\mathbf{q}}_M)$ which we shall study later.

2.3 The risk of the estimator

We compute the mean integrated squared error (MISE):

$$\begin{aligned} \mathbb{E}(\|\hat{f}_m - f\|_2^2) &= \|f - f_m\|_2^2 + \mathbb{E}(\|\hat{f}_m - f_m\|_2^2) \\ &= \|f - f_m\|_2^2 + \mathbb{E}(\|\widehat{\mathbf{f}}_m - \mathbf{f}_m\|^2) \\ &= \|f - f_m\|_2^2 + \mathbb{E}(\|\widehat{\mathbf{f}}_m - \mathbb{E}(\widehat{\mathbf{f}}_m)\|^2) + \|\mathbb{E}(\widehat{\mathbf{f}}_m) - \mathbf{f}_m\|^2 \end{aligned} \quad (2.8)$$

The first term in the right-hand side of (2.8) is the functional approximation bias resulting from replacing f by its expansion over the finite system of Laguerre functions $(\phi_0, \dots, \phi_{m-1})$. The second term is the variance term. The last term represents the additional bias which is due to estimation of the coefficients in the orthonormal basis, defined on the positive real line, using a finite number of data points that are sampled on a finite interval $[0, T]$. In order to control this last term, we

introduce the following assumption [†] :

(A0): For some $C_q > 0$, one has $\sum_{k \geq 0} [k^2 q^{(k)}]^2 \leq C_q < \infty$.

Denote

$$\mathbf{Q}_m = \frac{n}{T} [(\Phi_M^T \Phi_M)^{-1}]_m ([\mathbf{G}_M \mathbf{G}_M^T]_m)^{-1}.$$

Then, the following statement is true.

Proposition 1. *Set $M = M(n) = n^{(1+\eta)/3}$ where $0 < \eta < 2$. If Assumption (A0) holds and $n \geq (2aC_q/\sigma^2)^{1/\eta}$, then,*

$$\mathbb{E}(\|\hat{f}_m - f\|_2^2) \leq \|f - f_m\|_2^2 + \frac{4}{3} \frac{\sigma^2 T}{n} \text{Tr}(\mathbf{Q}_m) \quad (2.9)$$

and therefore

$$\|f - f_m\|_2^2 + \frac{\sigma^2 T}{n} \text{Tr}(\mathbf{Q}_m) \leq \mathbb{E}(\|\hat{f}_m - f\|_2^2) \leq \|f - f_m\|_2^2 + \frac{4}{3} \frac{\sigma^2 T}{n} \text{Tr}(\mathbf{Q}_m) \quad (2.10)$$

The proofs of this and the later statements are presented in Section 8, Proofs, or in Appendix A.

Remark 1. The choice of the value of η in Proposition 1 depends on how large the number of observations n is. The medium value $\eta = 1$ corresponds to the very moderate requirement $n \geq 2aC_q/\sigma^2$ on the value of n . If n is relatively large, one can reduce η and, therefore, M since smaller values of M lead to more stable computations. For instance, if one selects $M(n) = n^{1/2}$, then $\eta = 1/2$ and the estimator is fully adaptive as long as $n \geq (2aC_q/\sigma^2)^2$.

We define the set of indices

$$\mathcal{M}_n = \{1, \dots, M\}. \quad (2.11)$$

The smallest possible risk, the so-called *oracle* risk, is obtained by minimizing the left-hand side of expression (2.10) with respect to m :

$$R_{\text{oracle}} = \min_{m \in \mathcal{M}_n} [\|f_m - f\|_2^2 + \sigma^2 T n^{-1} \text{Tr}(\mathbf{Q}_m)]. \quad (2.12)$$

Hence, the objective is to choose a value of $m \in \mathcal{M}_n$ which delivers an estimator of the unknown function f with the risk as close as possible to the oracle risk or at least to the right-hand side of (2.12). Since the bias term $\|f_m - f\|_2^2$ is unknown, in order to attain this goal, one can use a penalized version of estimator (2.6) as it is described in the next section.

2.4 Selection of the model size via penalization

Denote

$$\mathbf{A}_m = \sqrt{\frac{n}{T}} \mathbf{G}_m^{-1} \mathbf{J}_{m,M} (\Phi_M^T \Phi_M)^{-1} \Phi_M^T. \quad (2.13)$$

[†] Assumption (A0) requires q defined by (1.3) to be smooth and decline as $t \rightarrow +\infty$. More precisely, if $a = 1/2$ for simplicity, it is sufficient that $\mathcal{L}^2 q \in \mathbb{L}^2(\mathbb{R}^+)$ where the differential operator \mathcal{L} is defined as

$$\mathcal{L}u = - \left[t \frac{d^2}{dt^2} + \frac{d}{dt} - \frac{t}{4} \right] u.$$

For details on Sobolev spaces associated to Laguerre functions, see Bongioanni and Torrea (2009), or Vareschi (2015).

and

$$v_m^2 := \|\mathbf{A}_m\|_2^2 = \text{Tr}(\mathbf{Q}_m), \quad \rho_m^2 := \lambda_{\max}(\mathbf{A}_m^T \mathbf{A}_m) \quad (2.14)$$

Introduce the penalty

$$\text{pen}(m) := 8\sigma^2 T n^{-1} [v_m^2 + 2\kappa \rho_m^2 \log(m \rho_m / \rho_1)], \quad (2.15)$$

where $\kappa = 1$ for Gaussian errors ε_i and κ is the squared sub-gaussian norm of ε_i , otherwise (see the definition in Vershynin (2012)). The value $\rho_1 = \mathbf{A}_1^T \mathbf{A}_1 = \|\mathbf{A}_1\|^2$ is the squared norm of vector \mathbf{A}_1 and is necessary to account for the scale parameter a .

For each $m = 1, \dots, M$, consider the estimator \hat{f}_m of f of the form (2.4) where the coefficients $\hat{\mathbf{f}}_m$ are defined by (2.6). This estimator appears as the least squares estimator with the contrast equal to $-\|\hat{\mathbf{f}}_m\|^2$. For selecting the model size m , we search for \hat{m} which minimizes the sum of the penalty and the contrast

$$\hat{m} := \arg \min \left\{ m \in \mathcal{M}_n : -\|\hat{\mathbf{f}}_m\|^2 + \text{pen}(m) \right\}. \quad (2.16)$$

and obtain the penalized least squares estimator $\hat{\mathbf{f}}_{\hat{m}}$ of the vector of Laguerre coefficients. Finally, we construct the estimator $\hat{f}_{\hat{m}}$ of f using Laguerre coefficients $\hat{\mathbf{f}}_{\hat{m}}$.

The heuristic argument behind this model selection procedure is the following. Since $\|f - f_m\|_2^2 = \|f\|_2^2 - \|f_m\|_2^2$, the bias-variance balance is attained by the value \hat{m} of m that delivers the minimum of $-\|f_m\|_2^2 + \text{Var}(\hat{f}_m)$. The term $\|f_m\|_2^2$ is estimated by $\|\hat{f}_m\|_2^2 = \|\hat{\mathbf{f}}_m\|^2$ and the variance term is approximated by $\text{pen}(m)$. Indeed, the following statement holds.

Theorem 1. *Let Assumption (A0) hold and $n \geq (2aC_q/\sigma^2)^{1/\eta}$. If $M = M(n) = n^{(1+\eta)/3}$, then one has*

$$\mathbb{E}(\|\hat{f}_{\hat{m}} - f\|_2^2) \leq \min_{m \in \mathcal{M}_n} \left[9\|f_m - f\|_2^2 + 6\text{pen}(m) + 72\sigma^2 \rho_1^2 \frac{T}{mn} \right]. \quad (2.17)$$

Since $\rho_m^2 \leq v_m^2$ for any value of m , it follows from Theorem 1 that, for any value of m , the risk of the estimator $\hat{f}_{\hat{m}}$ lies within a logarithmic factor of the upper bound of oracle risk defined in (2.12). Note that the upper bound in Theorem 1 is non-asymptotic and holds for any values of T and n and any distribution of points t_i , $i = 1, \dots, n$. In particular, the following corollary is valid.

Corollary 1. *Under conditions of Theorem 1, one has*

$$\mathbb{E}(\|\hat{f}_{\hat{m}} - f\|_2^2) \leq 48[1 + 2\kappa \log(m_0 \rho_{m_0} / \rho_1)] R_{\text{oracle}} + 96\sigma^2 \rho_1^2 \frac{T}{m_0 n}, \quad (2.18)$$

where $m_0 = m_0(n, T)$ is the value of m delivering the minimum in the right-hand side of (2.17).

3 Asymptotic upper bounds for the risk and optimality of the estimator

Corollary 1 is valid for any function g and any distribution of sampling points, hence, it is true in the “worst case scenario”. It does not allow one to judge how fast the risk decreases when n grows. In particular, since the problem of Laplace deconvolution is an ill-posed problem, one needs to know how fast the error grows when m increases. Abramovich *et al.* (2013) addressed this question by showing that, under certain assumptions, the risk of the kernel density estimator grows as a

negative power of the bandwidth, so that the overall error tends to zero at a polynomial rate. In what follows, we introduce assumptions similar to those of Abramovich *et al.* (2013) and show that the MISE of the estimators produced by our methodology grows as a power of the model size, so that $\log(\varrho_m)$ is just a multiple of $\log m$. Moreover, we establish that the spectral and the Frobenius norms of matrix \mathbf{A}_m grow at the same rate as m increases.

3.1 Assumptions

Let $r \geq 1$ be such that

$$\left. \frac{d^j g(t)}{dt^j} \right|_{t=0} = \begin{cases} 0, & \text{if } j = 0, \dots, r-2, \\ B_r \neq 0, & \text{if } j = r-1, \end{cases} \quad (3.1)$$

with the obvious modification $g(0) = B_1 \neq 0$ for $r = 1$. Consider matrix

$$\mathbf{\Omega}_m := \frac{n}{T} [(\Phi_M^T \Phi_M)^{-1}]_m \quad (3.2)$$

and assume that function $g(x)$, its Laplace transform $G(s) := \int_0^{+\infty} e^{-sx} g(x) dx$, and matrix $\mathbf{\Omega}_m$ satisfy the following conditions.

- (A1) $g \in L_1[0, \infty)$ is r times differentiable with $g^{(r)} \in L_1[0, \infty)$.
- (A2) Laplace transform $G(s)$ of g has no zeros with nonnegative real parts except for zeros of the form $s = \infty + ib$.
- (A3) There exists n_0 such that, for $n > n_0$, eigenvalues of matrix $\mathbf{\Omega}_m$ are uniformly bounded, i.e.

$$0 < \lambda_1 \leq \lambda_{\min}(\mathbf{\Omega}_m) \leq \lambda_{\max}(\mathbf{\Omega}_m) \leq \lambda_2 < \infty \quad (3.3)$$

for any $m = 1, \dots, M$, and some absolute constants λ_1 and λ_2 .

Consider, for example,

$$g_1(t) = e^{-5t}(2t - \sin(2t)), \quad g_2(t) = e^{-5t}, \quad g_3(t) = e^{-t}(2t + 1), \quad (3.4)$$

Then, $g_1(t) = e^{-5t}(2t - \sin(2t))$ and then $g_1(0) = g_1'(0) = g_1''(0) = 0$ and $g_1'''(0) = 8$, so that $r = 4$ for g_1 and $r = 1$ for g_2 and g_3 . One can also easily evaluate Laplace transforms $G_1(s) = 8(s+5)^{-2}[(s+5)^2 + 4]^{-1}$, $G_2(s) = (s+5)^{-1}$ and $G_3(s) = (s+1)^{-2}(s+3)$. Hence, functions $G_1(s)$ and $G_2(s)$ do not have zeros and $G_3(s)$ has a single zero $s_1 = -3$ with a negative real part. Later, we shall use the kernels (3.4) in our simulation study.

Definition of r and Assumptions (A1) and (A2) are similar to those introduced in Abramovich *et al* (2013). Assumption (A1) requires $g(t)$ to have r derivatives and to decline as $t \rightarrow \infty$. Assumption (A2) establishes that the Toeplitz matrix does not have eigenvalues that decrease exponentially as the functions of the matrix dimension. Finally, Assumption (A3) ensures that the design points t_i , $i = 1, \dots, n$, are relatively regularly spaced on the interval $[0, T]$. The normalization of $\mathbf{\Omega}_m$ by T/n is justified by the fact that the matrix tends to the identity matrix when both n and T tend to infinity. Assumption (A3) also implies that $M \leq n$.

Observe that, if g is known exactly, all assumptions are set on known quantities. If g is known only approximately (or is estimated from data as in the case of DCE imaging), the value of r and the locations of zeros of $G(s)$ are hard to determine. However, Assumption (A3) is independent of g and can always be verified. In particular, one can compute matrices $\mathbf{\Omega}_m$ and find their lowest and highest eigenvalues λ_1 and λ_2 . Nevertheless, unlike in Abramovich *et al* (2013), our estimation technique does not rely on the knowledge of r or $G(s)$, so that the risk satisfies the oracle inequalities (2.17) and (2.18) whether we know those quantities or not.

3.2 Asymptotic near-optimality of the estimators

From properties of Toeplitz matrices that are reviewed in the Appendix, it follows that under Assumptions **(A1)**–**(A3)**, both v_m^2 and ρ_m^2 are polynomial in m . Moreover, Lemma 4 presented in Appendix (Section A) shows that, for m large enough, one has

$$C_1 m^{2r} \leq \rho_m^2 \leq v_m^2 \leq C_2 m^{2r}, \quad (3.5)$$

for some absolute positive constants C_1 and C_2 , exact values of which are presented in Lemma 4. Hence, Lemma 4 implies that, in (2.15), $\rho_m^2 \log(m\rho_m/\rho_1) \propto v_m^2 \log(m)$ as $m \rightarrow \infty$, so that the second term in (2.15) is almost of the same asymptotic order as the first term, up to at most $(\log n)$ factor. Consequently, as $n \rightarrow \infty$ and $T/n \rightarrow 0$, the right-hand side of (2.17) is of almost the same asymptotic order as the oracle risk (2.12). Thus, by combination of Theorem 1 and Lemma 4, we obtain to the following statement.

Theorem 2. *Under assumptions **(A0)**–**(A3)**, for an estimator $\hat{f}_{\hat{m}}$ of f with penalty given by equation (2.15), as $n \rightarrow \infty$,*

$$\frac{R(\hat{f}_{\hat{m}})}{R_{\text{oracle}}} \leq C(r) \log n [1 + o(1)], \quad (3.6)$$

provided $T/n \rightarrow 0$ as $n \rightarrow \infty$. Here, $C(r)$ is a constant that depends on r only.

Remark 2. The theory above is valid for T being finite as well as for $T = T_n \rightarrow \infty$ as long as $T_n/n \rightarrow 0$ as $n \rightarrow \infty$. Indeed, the natural consequence of T being finite is that the bias term $\|f - f_m\|_2^2$ might be relatively large due to misrepresentation of f for $t > T$. However, since both the risk of the estimator $R(\hat{f}_{\hat{m}})$ and the oracle risk are equally affected, Theorem 2 remains valid whether $T = T_n$ grows with n or not.

4 Motivation: perfusion imaging and DCE imaging data

Cancers and vascular diseases inducing stroke and heart infraction present major public health concerns. Considerable improvement in assessing the quality of a vascular network and its permeability have been achieved through perfusion imaging using Dynamical Contrast Enhanced (DCE) imaging procedures with either Computer Tomography (DCE-CT), Magnetic Resonance Imaging (DCE-MRI) or Ultra Sound (DCE-US). The common feature of DCE imaging techniques is that each of them uses the rapid injection of a single dose of a bolus of a contrast agent and monitors its progression in the vascular network by sequential imaging. Currently, the high frequency DCE imaging techniques are more and more commonly used for medical assessment of brain flows for prognostic and therapeutic purposes after stroke, or, of cancer angiogenesis. They have a great potential for cancer detection and characterization, as well as for monitoring *in vivo* the effects of treatments (see, e.g., Cao (2011); Cao *et al.* (2010); Goh *et al.* (2005); Goh and Padhani (2007); Cuenod *et al.* (2006); Cuenod *et al.* (2011); Miles (2003); Padhani and Harvey (2005) and Bisdas *et al.* (2007)).

As an example, below we consider a DCE experiment which follows propagation, through the vascular network, of a bolus of a contrast agent, injected in a vein, after it passes through the heart. Assuming that all voxels have unit volumes, at a microscopic level, for a given tissue voxel of interest, the number of arriving particles at time $t + \delta$ is given by $\beta \text{AIF}(t)$. Here, $\text{AIF}(t)$ is the Arterial Input Function that measures concentration of the contrast agent within the tissue voxel inside the aorta at time t , and parameter β , the so-called *Tissue Blood Flow*, is the proportion of the contrast agent which enters this voxel. Denote the number of particles in the tissue voxel at

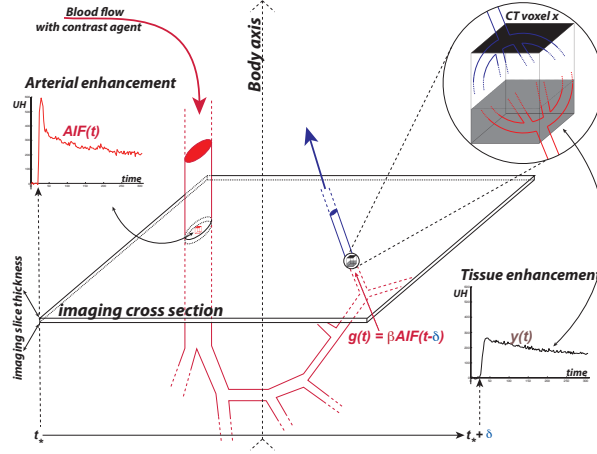


Figure 1: DCE imaging experiment and contrast agent circulation. Figure shows a sub-tree of the vascular system going from the artery –which receives oxygenated blood (red arrow)– to the vein –which returns the de-oxygenated blood (blue arrow) after exchanges within the tissue. After passing through the heart, the bolus of the contrast agent, injected into a vein, is distributed, throughout the body along the arterial network to the tissue and later back to the venous system. In the imaging cross-section, the contrast agent induces enhancements first in the artery, providing the AIF, and later in the tissue of interest providing observations $y(t_i)$, $i = 1, \dots, n$. Enhancements are measured in the voxels of the imaging cross-section.

time t by $y(t)$ and the random lapse of time during which a particle sojourns in the tissue voxel by S . Assuming sojourn times for different particles to be independent and identically distributed with a cumulative distribution function F , one obtains the following equation for the average number of particles of the contrast agent in the tissue voxel at the moment t

$$\mathbb{E}y(t) = \underbrace{\int_0^{t-\delta} \beta \text{AIF}(t-\tau) d\tau}_{\text{arrived before time } t} - \underbrace{\int_0^{t-\delta} \beta \text{AIF}(t-\tau) P(S \leq \tau) d\tau}_{\text{left before time } t} = \int_0^{t-\delta} \text{AIF}(t-\tau) \beta(1-F(\tau)) d\tau,$$

where the expectation is taken under the unknown distribution of the sojourn times and δ is the delay between the measurement of the concentration of the contrast agent inside the aorta and its arrival inside the tissue voxel of interest. Assuming that the transit inside the arteries is homogeneous, up to parameter δ , the aorta acts as a good proxy of the feeding artery of the voxel of interest. In reality, one does not know $\mathbb{E}y(t)$ and has discrete noisy observations

$$y(t_i) = \mathbb{E}y(t_i) + \sigma \varepsilon_i,$$

where ε_i are i.i.d. standardized random variables.

Medical doctors are interested in a reproducible quantification of the blood flow inside the tissue which is characterized by $f(t) = \beta(1-F(t))$ since this quantity is independent of the concentration of particles of contrast agent within a voxel inside the aorta described by $\text{AIF}(t)$. The sequential imaging acquisition is illustrated by Figure 1. The contrast agent arrives with the oxygenated blood through the aorta (red arrow) where its concentration, AIF, within unit volume voxel is measured first when it passes through the imaging cross-section (red box). Subsequently, the contrast agent enters the arterial system, and it is assumed that its concentration does not change during this phase. The exchange within the tissue of both oxygen and contrast agent occurs from the beginning of the feeding phase and the concentration of contrast agent during this exchange is measured in

all tissue voxels inside the imaging cross-section (grey voxel in the zoom). Later the contrast agent returns to the venous system with the de-oxygenated blood (blue arrow).

This leads to the following complete observation model:

$$y(t_i) = \int_0^{t_i-\delta} \text{AIF}(t_i - \tau) \beta(1 - F(\tau)) d\tau + \sigma \varepsilon_i, \quad i = 1, \dots, n, \quad (4.7)$$

$$\eta(t_i) = \text{AIF}(t_i) + \sigma_0 \xi_i, \quad j = 1, \dots, m, \quad (4.8)$$

where ξ_i , are i.i.d. centered random variables independent from the ε_j , $j = 1, \dots, n$. The value of delay δ can be measured with a small error using the delay between the moment when the contrast agent appears inside the aorta and the time it appears in the voxel of interest – both being measured in the imaging cross section. For this reason, in what follows, we assume that the time measurements are appropriately shifted, so that we can use $\delta = 0$ in (4.7). Unfortunately, evaluation of the proportion β is a much harder task and, hence, is realized with a much larger error. Mathematically, it corresponds to estimation of the value of f at $t = 0$ since $F(0)$ is always zero.

In addition, a large artery, like the aorta, when available in the imaging field, usually covers a Region Of Interest (ROI) of few hundreds voxels. In this case, the observed value $\eta(t_i)$ is obtained by averaging (at each time t_i) of the values observed in the ROI leading to $\sigma_0 \ll \sigma$, so that we can assume that $\sigma_0 = 0$. Therefore, the complete model (4.7) for DCE imaging experiments reduces to the Laplace convolution equation based on noisy observations of the form (1.1), the study of which presents a necessary theoretical step before obtaining medical answers on the basis of the model (4.7). Nevertheless, we draw attention to the fact that, in the DCE context, $\text{AIF}(t)$ is only available at the observation times t_i , $i = 1, \dots, n$.

5 Simulation study

In this section we present the results of a simulation study to illustrate finite sample performance of the Laplace deconvolution procedure developed above. In what follows, we compare our method with the one introduced in Abramovich *et al.* (2013), since, to the best of our knowledge, it is the only competitive method specifically designed for solution of Laplace convolution equation in the presence of noise. We also carried out comparisons with the standard techniques designed for solution of general ill-posed linear inverse problems, namely, the Tikhonov regularization and the Singular Value Decomposition (tSVD).

Moreover, we put our best effort to apply the Laplace transform inversion of the numerical realization of the Laplace transform of our equation suggested by Mnatsakanov (2011) and Mnatsakanov and Sarkisian (2013) but failed to produce any reasonable results due to the small sample sizes ($n \leq 250$).

Settings

We used two different simulation settings. In the first one, an analytic form of g is known, so that the estimator \hat{f}_{APR} developed in Abramovich *et al.* (2013) is available. In the second setting, only $g(t_1), \dots, g(t_n)$ are known, so that one cannot construct \hat{f}_{APR} . In both setting, we considered Gaussian noise in (1.1) and set $\kappa = 1$ in (2.15).

Setting 1: g exactly known. We use the simulation set up of Abramovich *et al.* (2013). In particular, we considered fixed regular design with $T = 10$, sample sizes $n = 100$ and 250 , and three

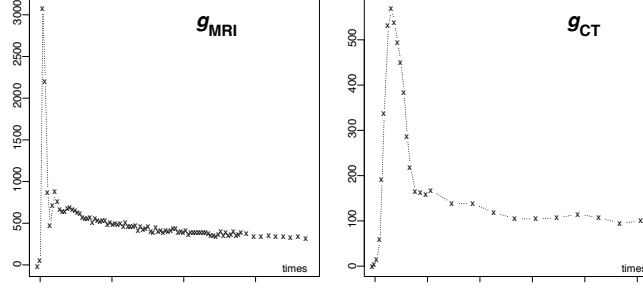


Figure 2: **DCE kernels:** (left) from a DCE-CT experiment ($n = 91$) and (right) from a DCE-MRI experiment ($n = 28$). Baselines are removed to access only the enhancements produce by the arrival of the bolus of the contrast agent. Crosses correspond to the observation times that are rescaled to the interval $[0, 10]$.

choices of the true function: $f_1(t) = t^2 e^{-t}$, $f_2(t) = 1 - \Gamma_{2,2}(t)$ and $f_3(t) = 1 - \Gamma_{3,0.75}(t)$, where $\Gamma_{\alpha,\theta}$ is the c.d.f of the Gamma distribution with the shape parameter α and the scale parameter θ . We used the five convolution kernels g_1, \dots, g_5 , where g_1, g_2 and g_3 are defined in (3.4) and kernels g_4 and g_5 are of the forms

$$g(t) = e^{-3t} t^2 \sum_{j=0}^k \frac{\rho_j}{(j+2)!} t^j, \quad \text{with} \quad G(s) = (s+3)^{-(k+3)} \sum_{j=0}^k \rho_j (s+3)^{k-j},$$

their Laplace transforms. Here, $\rho_0 = 1$; $k = 4$ and the numerator of $G(s)$ has four roots $(-4 \pm 2.5i, -0.75 \pm 1.5i)$ for g_4 ; $k = 6$ and the numerator of $G(s)$ has six roots $(-4 \pm 2.5i, -0.75 \pm 1.5i, -2 \pm 2i)$ for g_5 . Both g_4 and g_5 are such that $r = 3$ in (3.1). For each kernel, we chose the nominal noise levels $\sigma_0(g_j)$ that were, respectively, equal to 0.001, 0.1, 0.01, 0.002, 0.002 for g_1, \dots, g_5 . Simulations were carried out with noise levels $\sigma_0(g_j)/2^i$, $i = 1, \dots, 5$.

Setting 2: observations of g are available. We consider two “real life” kernels, g_{MRI} and g_{CT} , obtained, respectively, from a DCE-MRI ($n = 91$) and a DCE-CT ($n = 28$) sequences of one patient. For those kernels, shown in Figure 2, only $g(t_i)$, $i = 1, \dots, n$ are observed and no analytical form of g is available. In (4.7), we chose $\beta = 0.5$ and f_2, f_3 and $f_4(t) = \exp(-2t)$ as test functions, since they correspond to typical survival functions $1 - F$. For each test function, we computed the function q at the time points t_i , $i = 1, \dots, n$, in (1.2) by numerical integration with trapezoid rule. Then we added Gaussian noise with realistic noise levels, namely, $\sigma = 60$ for g_{MRI} and $\sigma = 25$ for g_{CT} .

Implementation

In order to implement our procedure and to stay as close as possible to the real-life DCE imaging experiments, we only used the knowledge of the vector $\vec{g} = (g(t_1), \dots, g(t_n))^T$ of values of $g(t)$ at the points t_1, \dots, t_n . The elements of matrix \mathbf{G}_M are derived from $\widehat{\mathbf{g}}_M$, the linear regression estimators of the Laguerre coefficients of g , obtained as $\widehat{\mathbf{g}}_M = (\Phi_M^T \Phi_M)^{-1} \Phi_M^T \vec{g}$, similarly to (2.5).

We implement our procedure using the public software *R*. Numerical computations using Laplace functions are facing numerical instabilities when M is too large. Hence, for a given kernel g and for each value a , we selected the largest value of $M \leq 25$ such that both matrices $\Phi_M^T \Phi_M$

and $\widehat{\mathbf{G}}_M \widehat{\mathbf{G}}_M^T$ are of full rank and set $M(n) = M$ in (2.11) and Proposition 1. For the sample sizes $n = 100, 250, 91$ and 28 , used in our simulation settings, this leads to $\eta = 1.10, 0.75, 1.14$ and 1.90 , respectively in Proposition 1 and Theorem 1.

Subsequently, we derived \widehat{m} using (2.16) and obtained the penalized estimator $\widehat{\mathbf{f}}_{\widehat{m}}$ of the vector of Laguerre coefficients. We evaluated the estimator $\widehat{q} = \widehat{q}(a)$ on the basis of the estimator $\widehat{\mathbf{f}}_{\widehat{m}}$. At last, we chose the value of a which minimizes the Euclidean norm $R(a)$ of the difference between \vec{y} and the vector $\widehat{q}(a)$.

Competing techniques

We compared our procedure (referred to as \widehat{f}_{LAG} with the estimator introduced in Abramovich *et al.* (2013), (denoted \widehat{f}_{APR} below) as well as with the Tikhonov regularization ($\widehat{f}_{\text{TIKH}}$) and the Singular Value Decomposition ($\widehat{f}_{\text{tSVD}}$). To this end, we rewrote equation (1.1) using trapezoidal approximation of the integral $\int_0^t g(t-\tau)f(\tau)d\tau$, thus, realizing the Laplace convolution as $\vec{q} \approx A\vec{f}$ where A is the lower triangular matrix. We considered the SVD of A , $A = U S V^T$ where, respectively, S is a diagonal and U and V are orthogonal matrices. Then, the Tikhonov regularization -based estimator is given by

$$\widehat{f}_{\text{TIKH}} = V S (S^2 + \lambda I)^{-1} U^T U^T \vec{y} \quad (5.9)$$

The SVD estimator is defined as

$$\widehat{f}_{\text{tSVD}} = V (S_k)^{-1} U^T \vec{y}, \quad (5.10)$$

where S_k is the diagonal matrix derived from S by setting its k smallest components to infinity, so they vanish in $(S_k)^{-1}$. The values of parameters λ in (5.9) and k in (5.10) are obtained by minimizing the Euclidean norm of the difference between \widehat{q} (reconstructed from, respectively, $\widehat{f}_{\text{TIKH}}$ and $\widehat{f}_{\text{tSVD}}$), and an estimated version \tilde{q} of q obtained from y by local polynomial regression fitting.

Results of simulations

For each simulation, given an estimator \widehat{f} of f at times $0 = t_1 \leq \dots \leq t_n = T$, in order to take into account the possibly irregular design, we computed the Integrated Square Errors, $ISE(\widehat{f})$ over the interval $[0, T]$ using the trapezoidal approximation of the integral. In each setting, we carried out 400 simulation runs. For each estimator, we calculated the average values of $ISE(\widehat{f})$ over those runs and the corresponding standard deviations.

Setting 1: g exactly known. Figure 3 presents the box-plots of the ratios $ISE(\widehat{f})/ISE(\widehat{f}_{\text{LAG}})$, constructed on the basis of 400 simulation runs, for \widehat{f} being \widehat{f}_{APR} , $\widehat{f}_{\text{TIKH}}$ and $\widehat{f}_{\text{tSVD}}$, $n = 100$ and noise levels $\sigma_0(g_j)/2^i$ for $i = 1, 3, 5$. The empirical risk ratios are represented on a \log_{10} -scale: horizontal lines provide the references to the decibels (dB). The plain red line, showing 0dB, corresponds to the equal error for our estimator and its competitor. All values above this line suggest that our estimator has a smaller error. The box-plots confirm that, except for a few rare cases (where the ratio is very close to one), our estimator outperforms its competitors for all choices of kernels and test functions, and for all sample sizes and all noise levels. Similar results were obtained for other noise levels and for $n = 250$.

Figure 4 presents the graphs of \widehat{f}_{LAG} together with \widehat{f}_{APR} for all test functions and kernels g_j when the noise level is $\sigma_0(g_j)/2$. It is easy to see that, in all cases, \widehat{f}_{LAG} shows a much more stable behavior than \widehat{f}_{APR} on the boundaries. The figures report the values of the ISE over the whole interval $[0, T]$ and also over 80% of its interior points. The overall error of \widehat{f}_{LAG} is always

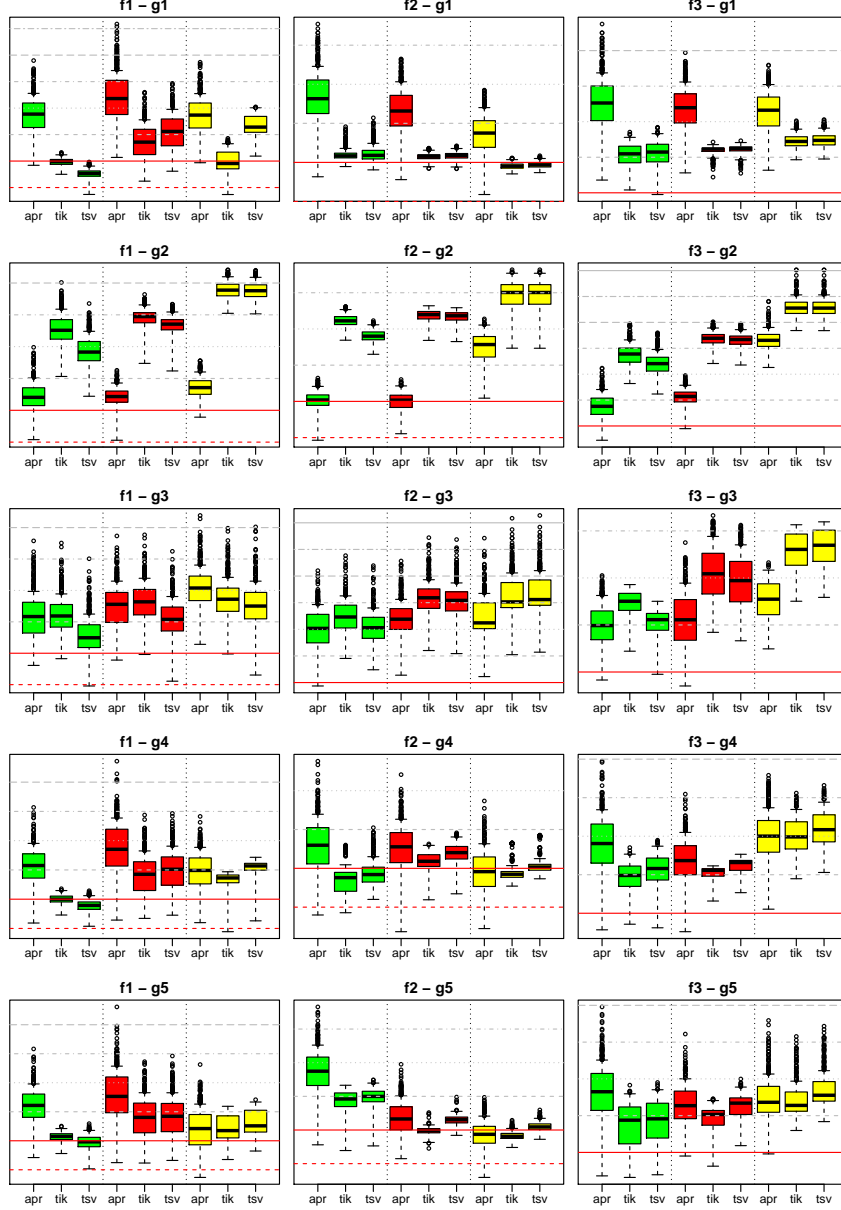


Figure 3: **Box-plots of $ISE(\hat{f})/ISE(\hat{f}_{LAG})$** for \hat{f} being \hat{f}_{APR} , \hat{f}_{TIKH} , \hat{f}_{TSVD} with $n = 100$ and noise levels $\sigma_0(g_j)/2^i$ for $i = 1$ (green), $i = 3$ (red) and $i = 5$ (yellow). The box-plots are constructed on the basis of 400 simulation runs. In each column, kernels g vary from g_1 (top) to g_5 (bottom). In each row, unknown function f vary from f_1 (left) to f_3 (right). The empirical risk ratios are represented on a \log_{10} -scale: horizontal lines provide the references to the decibels (dB). The plain red line, showing 0dB, corresponds to the equal error for our estimator and its competitor. All values above this line suggest that our estimator has a smaller error. Other horizontal dashed lines provides positive (grey) or negative (red) increments of 1dB.

overwhelmingly smaller than that of \hat{f}_{APR} . In the interior of the interval, \hat{f}_{APR} is competitive but the errors are extremely small for both estimators. We also remind that \hat{f}_{APR} cannot handle the case when g is not known exactly and, hence, is not used for comparisons in Setting 2.

To conclude this first set of simulations, Table 1 in the Appendix provides the average values of $ISE(\hat{f}_{LAG})$ computed over 400 simulation runs together with their standard deviations (in italic).

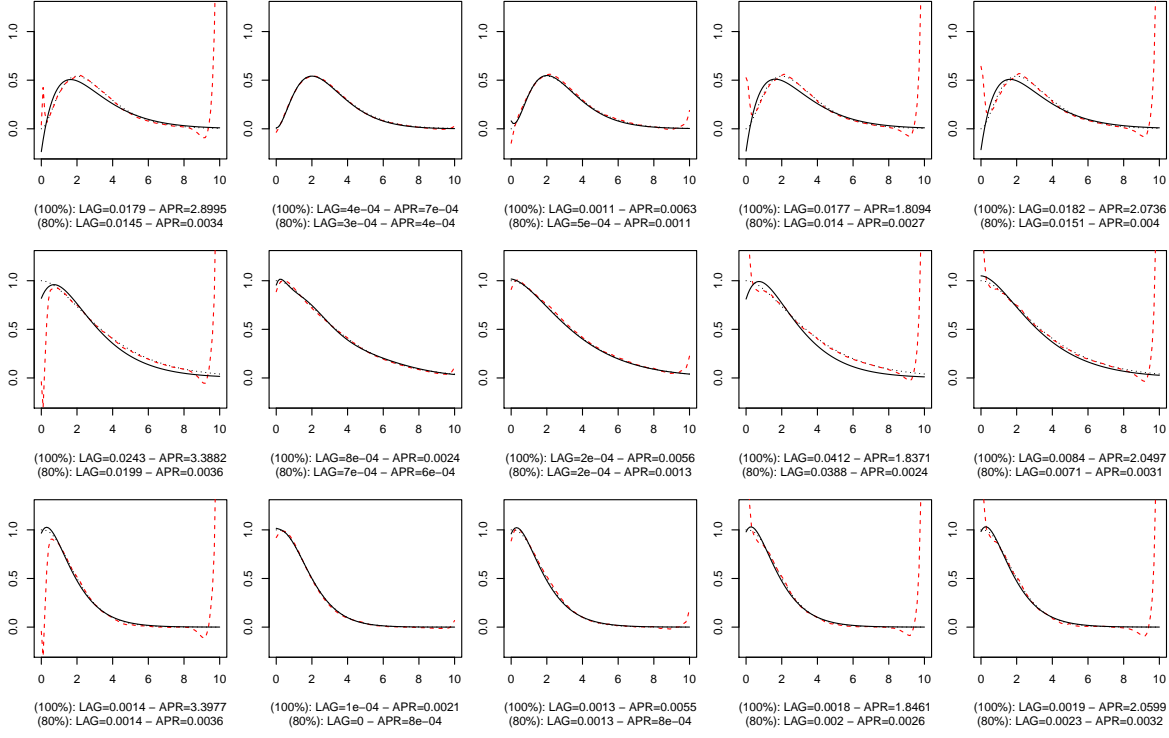


Figure 4: **Graphs of \hat{f}_{APR} and \hat{f}_{LAG} .** One sample comparison with noise level $\sigma_0(g_j)/2$ and sample size $n = 100$. In each row, kernels g vary from g_1 (left) to g_5 (right). In each column, unknown function f vary from f_1 (top) to f_3 (bottom). In each sub-figure, the dotted line is the unknown test function, the dashed line is \hat{f}_{APR} and the plain line is \hat{f}_{LAG} . Below each sub-figure, we provide the values of $ISE(\hat{f}_{\text{LAG}})$ and $ISE(\hat{f}_{\text{APR}})$ over the whole interval $[0, T]$ and also over 80% of its interior points.

Setting 2: observations of g are available. In this setting, we compare performances of \hat{f}_{LAG} , \hat{f}_{TIKH} and \hat{f}_{SVD} . Figure 5 shows the graphs of the estimators obtained for each combination of kernel g and each test function f . Left and right columns correspond to, respectively, g_{MRI} and g_{CT} . From top to bottom, rows correspond to f_2 , f_3 and f_4 . In each column, the sub-figure on the left shows the values of $g(t_i)$ and $q(t_i)$ for $i = 1, \dots, n$, together with the reconstructed estimator \hat{q} obtained by convolution of \hat{f} and g , while the sub-figure on the right, displays the test function f together with \hat{f}_{LAG} , \hat{f}_{TIKH} and \hat{f}_{SVD} . Note that although the reconstructions \hat{q} based on \hat{f}_{LAG} , \hat{f}_{TIKH} and \hat{f}_{SVD} are very similar, the precisions of estimators \hat{f}_{LAG} , \hat{f}_{TIKH} and \hat{f}_{SVD} themselves is dramatically different, especially in the case of g_{MRI} (the right two columns). Note that \hat{q} is often used by radiologists as a visual indicator for the estimation quality. Figure 5 demonstrates, however, that this visual indicator is extremely poor and does not help in selection of an adequate deconvolution procedure.

In addition, for the DCE imaging setting, Figure 3 provides the box-plots of the ratios $ISE(\hat{f})/ISE(\hat{f}_{\text{LAG}})$, constructed over 400 simulation runs, for \hat{f} being \hat{f}_{TIKH} , \hat{f}_{SVD} , together, with the average values of $ISE(\hat{f}_{\text{LAG}})$ and their corresponding standard deviations. Figure 3 confirms that again \hat{f}_{LAG} outperforms \hat{f}_{TIKH} and \hat{f}_{SVD} in all settings.

Finally, Figure 7 studies estimation of β in (4.7), the Tissue Blood Flow parameter which is

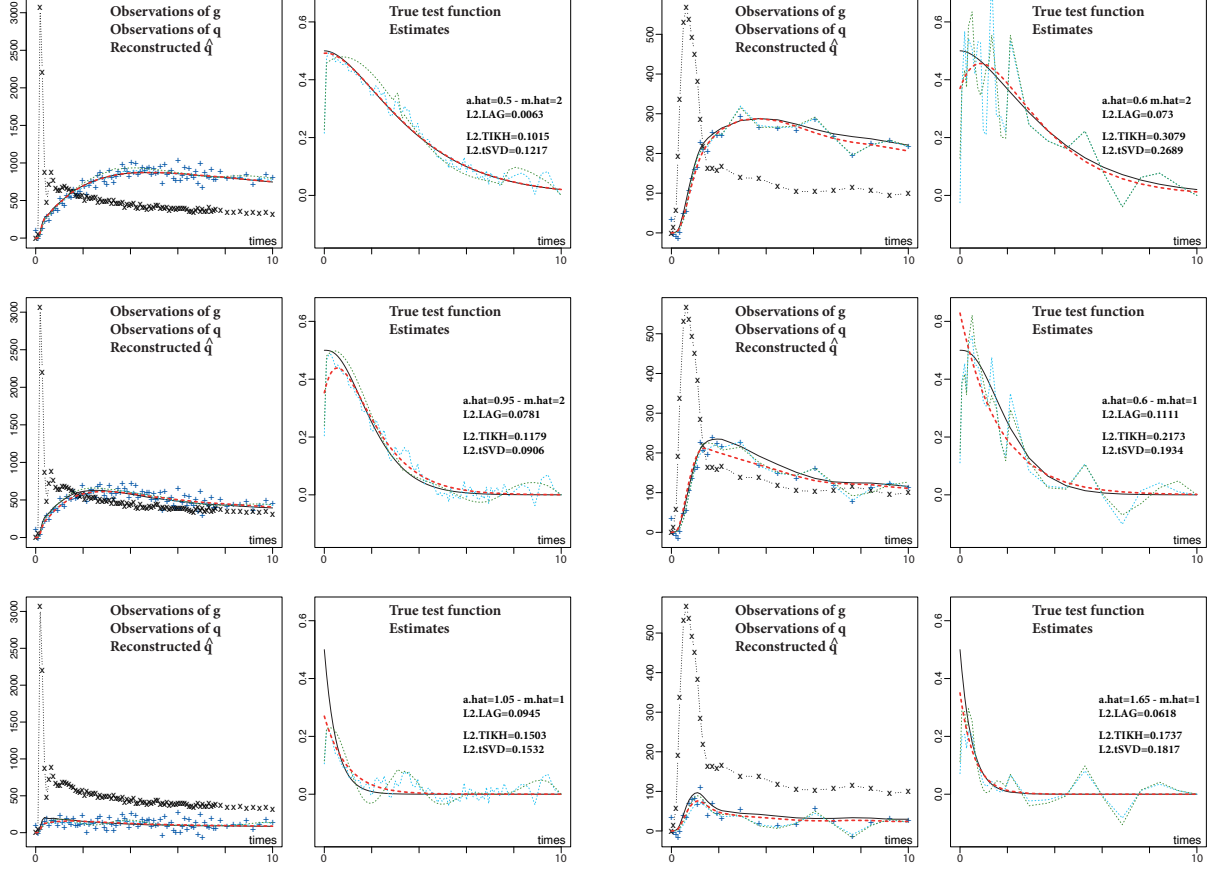


Figure 5: **Example of estimations in the DCE setting experiment:** Left and right column corresponds to, respectively, g_{MRI} and g_{CT} . From top to bottom, rows correspond to, respectively, f_2 , f_3 and f_4 . In each column, the sub-figures on the left represent observations $g(t_i)$ (black crosses \times) and $q(t_i)$ (blue crosses $+$) for $i = 1, \dots, n$, the unknown q (plain black line) and reconstructions \hat{q}_{LAG} (dashed red line), \hat{q}_{TIKH} (cyan dotted line) and \hat{q}_{tSVD} (dotted green line). The sub-figures on the right represent the true unknown test function f (plain black line) and its estimators \hat{f}_{LAG} (dashed red line), \hat{f}_{TIKH} (dotted cyan line) and \hat{f}_{tSVD} (plain green line).

of critical importance to radiologists and practitioners. Since $1 - F(0) = 1$, we use $\hat{\beta} = \hat{f}(0)$ as an estimator of β . Figure 7 presents boxplots of the values of $\hat{\beta}$ based on \hat{f}_{LAG} , \hat{f}_{TIKH} and \hat{f}_{tSVD} (constructed over 400 simulation runs). The red line indicates the true value $\beta = 0.5$ used in simulations. Our estimator performs better than its competitors and shows encouraging results for future applications in DCE imaging.

6 Real-life experiments

In order to apply our procedure to real data, we used two DCE-MRI sequences of one patient in the REMISCAN cohort study [40] who underwent anti-angiogenic therapy treatment for a metastatic renal carcinoma and showed positive response to the treatment after 3 months. The first sequence has been obtained just before the start of the treatment and the second 15 days later. One can notice that the first DCE-MRI sequence is more affected by the patient's movements: in spite of

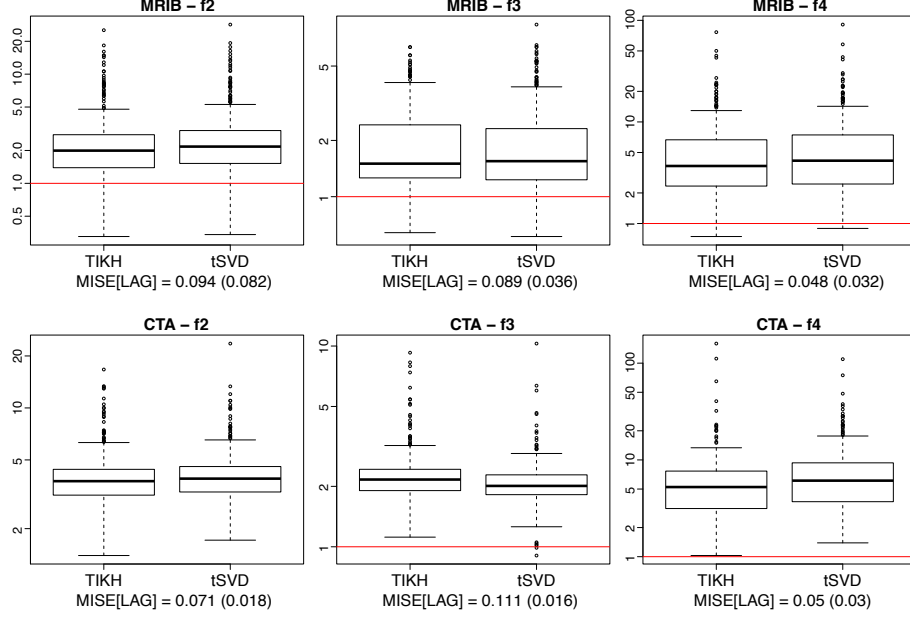


Figure 6: **Boxplot of the ratios $ISE(\hat{f})/ISE(\hat{f}_{LAG})$ for \hat{f} being \hat{f}_{TIKH} , \hat{f}_{tSVD} constructed over 400 simulation runs.** Upper row, g_{MRI} ($n = 91$, $\sigma = 75$). Lower row, g_{CT} ($n = 28$, $\sigma = 25$). From the left to the right column, test functions f_2 , f_3 and f_4 . For each boxplot, the average value of $ISE(\hat{f}_{LAG})$ and its corresponding standard deviations (in parenthesis) are provided.

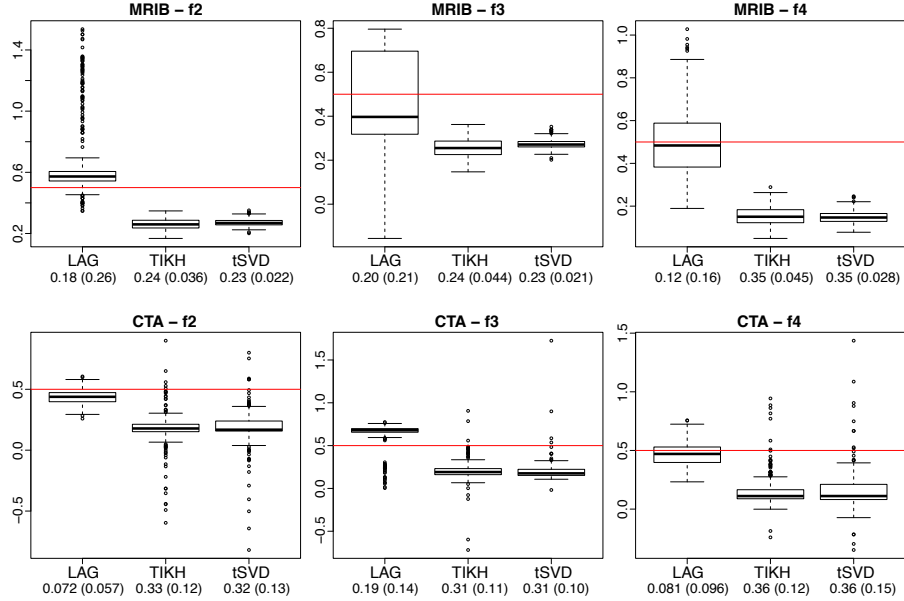


Figure 7: **Boxplot of $\hat{\beta} = \hat{f}(0)$ for \hat{f} being \hat{f}_{LAG} , \hat{f}_{TIKH} and \hat{f}_{tSVD} computed over 400 simulation runs.** Upper row: g_{MRI} ($n = 91$, $\sigma = 75$). Lower row: g_{CT} ($n = 28$, $\sigma = 25$). From the left to the right column: test functions f_2 , f_3 and f_4 . The red line corresponds to the true value of $\beta = 0.5$ used in simulations. The average values of $ISE(\hat{f}_{LAG})$ together with their corresponding standard deviations (in parentheses) are provided below each sub-figure.

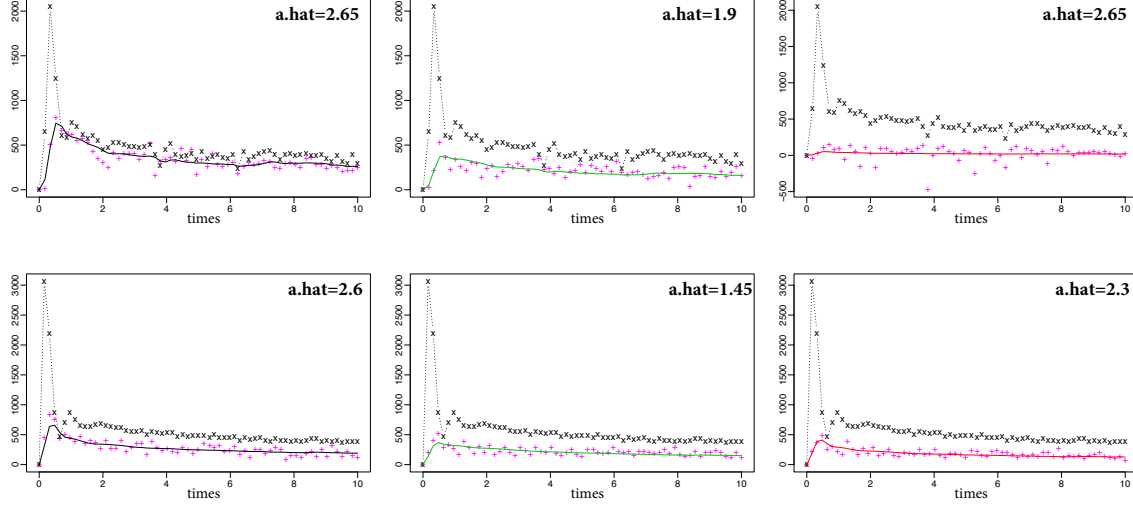


Figure 8: **The tissue enhancements (in the metastasis) (pink crosses +) and the corresponding AIFs (black crosses ×) obtained from two DCE-MRI sequences of the same patient in the REMISCAN cohort study.** Upper row corresponds to the DCE-MRI sequence obtained right before the start of the treatment; bottom row corresponds to the DCE-MRI sequence obtained 15 days after the treatment. The value \hat{a} chosen by cross-validation is provided in each sub-figure. The reconstructed enhancement \hat{q} (plain line), obtained after estimation, is displayed in each sub-figure as an indicator of the estimation precision.

being non-invasive, the first DCE-MRI experience is often stressful for a patient.

For each of $n = 91$ time instances, the DCE-MRI sequence is comprised of 16 slices (or images) of 256×256 voxels that cover the metastases and surrounding areas. Injection of the contrast agent was administered so that the arrival of the contrast agent occurred after about 10 acquisition times. For each sequence, the measurements before the arrival of the contrast agent were used to estimate the baseline image and its standard deviation σ . Then, the baseline was removed from the sequence in order to obtain the enhancements. Extra times before the arrival of the contrast agent were removed from the series and time was shifted, so that $t_1 = 0$, $AIF(t_1) \approx 0$ and $AIF(t_2) \gg 0$ and the effective sample size $n = 81$. The time shift δ in (4.7) was more or less constant and was treated as negligible for each sequence. Finally, we set $AIF(t_1) = y(t_1) = 0$ for $t < t_1$.

In each sequence, we selected three voxels inside the metastasis and obtained three enhancement curves. Since the aorta is visible on these DCE-MRI, its images were used for construction of estimators of the AIF that were obtained as the average enhancements for all (around 400) voxels in the aorta. The six tissue enhancements as well as the two denoised AIFs are presented in the Figure 8.

The corresponding estimates are shown in Figure 9. We remind that we estimate function $f = \beta(1 - F)$ in (4.7) where $(1 - F)$ is the survival function of the transit times of the contrast agent in the voxel and β is the Tissue Blood Flow parameter which can be estimated by $\hat{f}(0)$.

Before the treatment (upper line of Figure 8), the metastases exhibit three different spatial behaviors (hyper-vascular, vascular and necrotic) each illustrated by one of the three selected voxels: the enhancements correspond to the hyper-vascular (left), vascular (center) and necrotic (right) area. After 15 days of treatment (bottom line of Figure 8), three new voxels have been selected, one located in the hyper-vascular area observed before treatment (left), the two others located in the vascular area observed before treatment (center and right) to check for reproducibility.

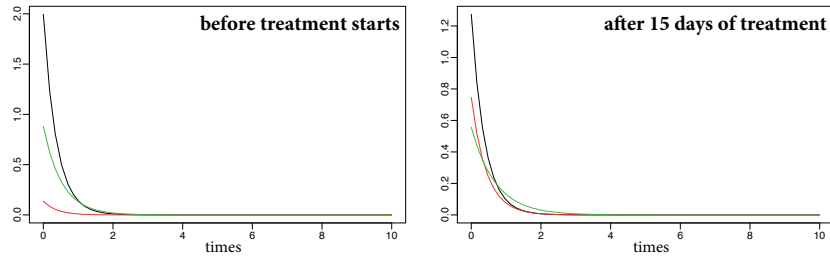


Figure 9: **DCE-MRI estimation results** The six estimates \hat{f} obtained from the enhancements for six voxels selected in the two DCE-MRI sequences obtained before the start of the treatment starts (left) and after 15 days of the treatment (right). The colors of the estimates correspond to the colors of the reconstructed enhancements in Figure 8.

In the left panel of Figure 9 corresponding to the DCE-MRI sequence obtained before treatment, one can observe that the estimators for the hyper-vascular (black curve) and vascular (green curve) voxels show similar shapes and, hence, similar time transit distributions but strong differences in the estimated Tissue Blood Flow parameters. Moreover, the estimated Tissue Blood Flow parameter for the voxel in the necrotic area (red curve) is, as expected, very small. In such poorly perfused tissues, one faces a small Signal to Noise Ratio (SNR) which challenges any deconvolution method. However, as simulations show, our technique is relatively robust to low SNR values.

In the right panel of Figure 9 corresponding to the DCE-MRI sequence obtained two weeks after the treatment, the estimator for the voxel located in the hyper-vascular area (black curve in the right panel) shows very similar shape to the estimator for the hyper-vascular voxel observed before the treatment (black curve in the left panel) but a much lower estimated Tissue Blood Flow parameter. This, however, can be expected as the result of the treatment which is aimed to reduce the Tissue Blood Flow. The estimators obtained after the treatment for the two voxels located in the vascular area look similar (red and green curves in the right panel) which is expected as they have been selected in a same area. Moreover, they also exhibit clear reduction of the Tissue Blood Flow parameters compared to the estimator for the vascular voxel before the treatment (green curve of left panel).

In conclusion, although we examined very limited experimental data, the estimators of the Tissue Blood Flow parameters and the survival functions show good reproducibility and are in accordance to what is expected by the clinicians.

7 Discussion

In the present paper, we study a noisy version of the Laplace convolution equation. Equations of this type frequently occur in various kinds of DCE imaging experiments. We propose an estimation technique for the solutions of such equation based on the expansion of the unknown solution, the kernel and the measured right-hand side over a system of the Laguerre functions. The number of the terms in the expansion of the estimator is controlled via complexity penalty. The technique leads to an estimator with the risk within a logarithmic factor of the oracle risk.

The major advantage of the methodology presented above is that it is practically usable, precise and computationally simple. Indeed, the expansion results in a small system of linear equations with the matrix of the system being triangular and Toeplitz. Therefore, the method is very easy and fast computationally and produces no boundary effects due to the extension at zero and the cut-off at T . In addition, application of the technique to discrete data does not require re-fitting the

model for each model size separately. On the contrary, the vector of the Laguerre coefficients of the observed function is fitted only once, for the largest model size, and then is truncated for models of smaller sizes. The complexity of representation of g adjusts to the complexity of representation of f and the noise level. Moreover, if g can be represented by a finite expansion over Laguerre functions with k terms, the matrix of the system is k -diagonal. The method performs very well in simulations. It is much more precise than the estimators described in Abramovich *et al.* (2013), as well as the estimators obtained by the SVD and the Tikhonov regularization.

Another important property of the method is that it can be easily applied when the kernel is not known exactly and is only observed at some points. This distinguishes the present technique from the approach of Abramovich *et al.* (2013) which strongly depends on the precise knowledge of the analytic form of the kernel and, hence, cannot be applied to solution of real-life problems. In the paper, we describe application of our methodology to analysis of the DCE-MRI sequences where the kernels are estimated on the basis of imaging data.

There are few more advantages which are associated with the use of Laguerre functions basis. Since one important goal of future analysis of DCE data is classification of the tissues and clustering of curves $f(t) = \beta(1 - F(t))$ which characterize their blood flow properties, representation of the curves via Laguerre basis allows to replace the problem of classification of curves by classification of relatively low-dimensional vectors. In addition, due to the absence of boundary effects, the method allows to estimate β , the Tissue Blood Flow parameter, which characterizes the micro-vascular properties of the tissue and is of extreme interest to medical doctors. Indeed, our simulations demonstrate that those estimators are fairly accurate. However, since they are based on a global estimator \hat{f}_{LAG} rather than on a local estimator at zero, there is some room for improvement. However, this issue is a matter of future investigation.

Acknowledgments

Marianna Pensky was partially supported by National Science Foundation (NSF), grants DMS-1106564 and DMS-1407475. The authors want to express sincere gratitude to Sergei Grudski for his invaluable help in the proof of Lemma 4 and very helpful discussions.

8 Proofs

8.1 Proof of Proposition 1

Recall that

$$\mathbb{E}(\|\hat{f}_m - f\|_2^2) = \|f - f_m\|_2^2 + \mathbb{E}(\|\hat{\mathbf{f}}_m - \mathbb{E}(\hat{\mathbf{f}}_m)\|^2) + \|\mathbb{E}(\hat{\mathbf{f}}_m) - \mathbf{f}_m\|^2 \quad (8.1)$$

The second term in (8.1) is the variance term which is equal to

$$\mathbb{E}(\|\hat{\mathbf{f}}_m - \mathbb{E}(\hat{\mathbf{f}}_m)\|^2) = \sigma^2 T n^{-1} \mathbb{E}[(\mathbf{A}_m \tilde{\varepsilon})^T \mathbf{A}_m \tilde{\varepsilon}] = \sigma^2 T n^{-1} \text{Tr}(\mathbf{A}_m^T \mathbf{A}_m)$$

with \mathbf{A}_m defined in (2.13). Observing that

$$\begin{aligned} \mathbf{J}_{m,M} (T n^{-1} \Phi_M^T \Phi_M)^{-1} \mathbf{J}_{m,M}^T \mathbf{G}_m^T \mathbf{G}_m^{-1} &= \frac{n}{T} [(\Phi_M^T \Phi_M)^{-1}]_m (\mathbf{G}_m \mathbf{G}_m^T)^{-1} \\ &= \frac{n}{T} [(\Phi_M^T \Phi_M)^{-1}]_m ([\mathbf{G}_M \mathbf{G}_M^T]_m)^{-1} = \mathbf{Q}_m, \end{aligned}$$

we obtain

$$\mathbb{E}(\|\hat{\mathbf{f}}_m - \mathbb{E}(\hat{\mathbf{f}}_m)\|^2) = \sigma^2 T n^{-1} \text{Tr}(\mathbf{Q}_m). \quad (8.2)$$

For the last term of right hand side of (2.8), we derive

$$\|\mathbb{E}(\widehat{\mathbf{f}}_m) - \mathbf{f}_m\|^2 = \|\mathbf{G}_m^{-1} \mathbf{J}_{m,M} (\Phi_M^T \Phi_M)^{-1} \Phi_M^T (\vec{q} - \vec{q}_M)\|^2.$$

Using inequality $\rho^2(\mathbf{A}) \leq \text{Tr}(\mathbf{A}^T \mathbf{A}) = \|\mathbf{A}\|_2^2$, and the fact that, for all $k \in \mathbb{N}$ one has $\|\phi_k\|_\infty \leq \sqrt{2a}$ (see Abramowitz and Stegun (1964), 22.14.12 and following), we bound this term by

$$\begin{aligned} \|\mathbb{E}(\widehat{\mathbf{f}}_m) - \mathbf{f}_m\|^2 &\leq \rho^2(\mathbf{G}_m^{-1} \mathbf{J}_{m,M} (\Phi_M^T \Phi_M)^{-1} \Phi_M^T) \|\vec{q} - \vec{q}_M\|_n^2 \\ &\leq \frac{T}{n} \text{Tr}(\mathbf{Q}_m) \sum_{i=1}^n (q(t_i) - q_M(t_i))^2 \\ &\leq \frac{T}{n} \text{Tr}(\mathbf{Q}_m) \sum_{i=1}^n \left(\sum_{k=M+1}^{\infty} q^{(k)} \phi_k(t_i) \right)^2 \\ &\leq \frac{T}{n} \text{Tr}(\mathbf{Q}_m) (2an) \left(\sum_{k=M+1}^{\infty} |q^{(k)}| \right)^2. \end{aligned} \tag{8.3}$$

Using Assumption **(A0)**, we obtain that

$$\left(\sum_{k=M+1}^{\infty} |q^{(k)}| \right)^2 = \left(\sum_{k=M+1}^{\infty} k^2 |q^{(k)}| k^{-2} \right)^2 \leq C_q \sum_{k=M+1}^{\infty} k^{-4} \leq C_q M^{-3}/3,$$

so that

$$\|\mathbb{E}(\widehat{\mathbf{f}}_m) - \mathbf{f}_m\|^2 \leq \frac{2aTC_q}{3} \frac{\text{Tr}(\mathbf{Q}_m)}{M^3}. \tag{8.4}$$

Combination of (8.1), (8.2) and (8.4) completes the proof of (2.9), provided that $M = n^{(1+\eta)/3}$ and $n \geq (2aC_q/\sigma^2)^{1/\eta}$.

8.2 Proof of Theorems 1 and 2

Proof of Theorem 1. For $m \in \mathcal{M}_n$, we consider the associated subspaces $S_m \subseteq \mathbb{R}^M$ defined by

$$\mathbf{t} \in S_m \text{ if } \mathbf{t} = (t^{(0)}, t^{(1)}, \dots, t^{(m-1)}, 0, 0, \dots, 0)^T.$$

For $\mathbf{t} \in S_m$, a vector of \mathbb{R}^M with at most its first m coordinates non-zero, $\widehat{\mathbf{f}}_m$ can be related to the minimizer over S_m of the contrast

$$\gamma_n(\mathbf{t}) = \|\mathbf{t}\|^2 - 2\langle \mathbf{t}, \mathbf{G}_M^{-1} \widehat{\mathbf{q}}_M \rangle.$$

Note that, for $\mathbf{t} \in S_m$,

$$\langle \mathbf{t}, \mathbf{G}_M^{-1} \widehat{\mathbf{q}}_M \rangle = \langle [\mathbf{t}]_m, \mathbf{G}_m^{-1} [\widehat{\mathbf{q}}_M]_m \rangle$$

where we recall that $[x]_m$ is the $m \times 1$ vector obtained by retaining the m first coordinates of x . Reciprocally, let us denote by $\mathbf{q}_{m,M}$, $\mathbf{f}_{m,M}$, and $\widehat{\mathbf{f}}_{m,M}$ the M -dimensional vectors where the first m elements coincide with the elements of m -dimensional vectors \mathbf{q}_m , \mathbf{f}_m , and $\widehat{\mathbf{f}}_m$ respectively, and the last $(M - m)$ elements are identical zeros. Since, for $\mathbf{t} \in S_m$, we have $\gamma_n(\mathbf{t}) = \|\mathbf{t} - \mathbf{G}_M^{-1} \widehat{\mathbf{q}}_M\|^2 - \|\mathbf{G}_M^{-1} \widehat{\mathbf{q}}_M\|^2$, we can see that clearly

$$\widehat{\mathbf{f}}_{m,M} = \arg \min_{\mathbf{t} \in S_m} \gamma_n(\mathbf{t}) \text{ and } \widehat{\mathbf{f}}_m = [\widehat{\mathbf{f}}_{m,M}]_m.$$

Now since $\gamma_n(\widehat{\mathbf{f}}_{m,M}) = -\|\widehat{\mathbf{f}}_{m,M}\|^2 = -\|\widehat{\mathbf{f}}_m\|^2$, we can see that

$$\widehat{m} = \arg \min_{m \in \mathcal{M}_n} \left\{ \gamma_n(\widehat{\mathbf{f}}_{m,M}) + \text{pen}(m) \right\}, \quad (8.5)$$

Let $m, m' \in \mathcal{M}_n$, $\mathbf{t} \in S_{m'}$ and $\mathbf{s} \in S_m$ and observe that

$$\gamma_n(\mathbf{t}) - \gamma_n(\mathbf{s}) = \|\mathbf{t} - \mathbf{f}_M\|^2 - \|\mathbf{s} - \mathbf{f}_M\|^2 - 2\langle \mathbf{t} - \mathbf{s}, \mathbf{G}_M^{-1} \widehat{\mathbf{q}}_M - \mathbf{f}_M \rangle, \quad (8.6)$$

where \mathbf{f}_M is the vector of the true M first Laguerre coefficients of function f . Note that, due to orthonormality of the Laguerre system, for any m ,

$$\|\widehat{f}_m - f\|_2^2 = \|\widehat{\mathbf{f}}_{m,M} - \mathbf{f}_M\|^2 + \sum_{j=M}^{\infty} \left(f^{(j)} \right)^2 \quad \text{and} \quad \|f_m - f\|_2^2 = \|\mathbf{f}_{m,M} - \mathbf{f}_M\|^2 + \sum_{j=M}^{\infty} \left(f^{(j)} \right)^2. \quad (8.7)$$

Now, the definition of \widehat{m} as given by (8.5) yields that for any $m \in \mathcal{M}_n$ one has

$$\gamma_n(\widehat{\mathbf{f}}_{\widehat{m},M}) + \text{pen}(\widehat{m}) \leq \gamma_n(\mathbf{f}_{m,M}) + \text{pen}(m),$$

which with (8.6), implies

$$\begin{aligned} \|\widehat{\mathbf{f}}_{\widehat{m},M} - \mathbf{f}_M\|^2 &\leq \|\mathbf{f}_{m,M} - \mathbf{f}_M\|^2 + \text{pen}(m) + 2\langle \widehat{\mathbf{f}}_{\widehat{m},M} - \mathbf{f}_{m,M}, \mathbf{G}_M^{-1} \widehat{\mathbf{q}}_M - \mathbf{f}_M \rangle - \text{pen}(\widehat{m}) \\ &\leq \|\mathbf{f}_{m,M} - \mathbf{f}_M\|^2 + \text{pen}(m) + 2\|\widehat{\mathbf{f}}_{\widehat{m},M} - \mathbf{f}_{m,M}\| \sup_{\mathbf{t} \in S_{\widehat{m} \vee m}} |\langle \mathbf{t}, \mathbf{G}_M^{-1} \widehat{\mathbf{q}}_M - \mathbf{f}_M \rangle| - \text{pen}(\widehat{m}). \end{aligned}$$

Due to $2xy \leq (x^2/\theta) + \theta y^2$ for all $x > 0, y > 0$ and $\theta > 0$, we get, choosing $\theta = 2$

$$\begin{aligned} \|\widehat{\mathbf{f}}_{\widehat{m},M} - \mathbf{f}_M\|^2 &\leq \|\mathbf{f}_{m,M} - \mathbf{f}_M\|^2 + \text{pen}(m) + \frac{1}{2} \|\widehat{\mathbf{f}}_{\widehat{m},M} - \mathbf{f}_{m,M}\|^2 \\ &\quad + 2 \sup_{\substack{\mathbf{t} \in S_{\widehat{m} \vee m} \\ \|\mathbf{t}\|=1}} \langle \mathbf{t}, \mathbf{G}_M^{-1} \widehat{\mathbf{q}}_M - \mathbf{f}_M \rangle^2 - \text{pen}(\widehat{m}). \end{aligned} \quad (8.8)$$

Due to $|x + y|^2 \leq (1 + \theta)x^2 + (1 + \theta^{-1})y^2$ for all x, y and $\theta > 0$, we get choosing $\theta = 3$,

$$\|\widehat{\mathbf{f}}_{\widehat{m},M} - \mathbf{f}_{m,M}\|^2 \leq \frac{4}{3} \|\widehat{\mathbf{f}}_{\widehat{m},M} - \mathbf{f}_M\|^2 + 4\|\mathbf{f}_{m,M} - \mathbf{f}_M\|^2, \quad (8.9)$$

and, choosing $\theta = 2$,

$$2 \sup_{\substack{\mathbf{t} \in S_{\widehat{m} \vee m} \\ \|\mathbf{t}\|=1}} \langle \mathbf{t}, \mathbf{G}_M^{-1} \widehat{\mathbf{q}}_M - \mathbf{f}_M \rangle^2 - \text{pen}(\widehat{m}) \leq \Delta_{m,\widehat{m}}^{(1)} + \Delta_{m,\widehat{m}}^{(2)} \quad (8.10)$$

where

$$\Delta_{m,\widehat{m}}^{(1)} = 3\sigma^2 \sup_{\substack{\mathbf{t} \in S_{\widehat{m} \vee m} \\ \|\mathbf{t}\|=1}} \langle \mathbf{t}, \mathbf{G}_M^{-1} (\Phi_M^T \Phi_M)^{-1} \Phi_M^T \bar{\varepsilon} \rangle^2 - \frac{3}{4} \text{pen}(\widehat{m}),$$

$$\Delta_{m,\widehat{m}}^{(2)} = 6 \sup_{\substack{\mathbf{t} \in S_{\widehat{m} \vee m} \\ \|\mathbf{t}\|=1}} \langle \mathbf{t}, \mathbf{G}_M^{-1} (\Phi_M^T \Phi_M)^{-1} \Phi_M^T (\vec{q} - \vec{q}_M) \rangle^2 - \frac{1}{4} \text{pen}(\widehat{m}).$$

Plugging (8.9) and (8.10) into (8.8) yields

$$\frac{1}{3} \|\widehat{\mathbf{f}}_{\widehat{m},M} - \mathbf{f}_M\|^2 \leq 3\|\mathbf{f}_{m,M} - \mathbf{f}_M\|^2 + \text{pen}(m) + \Delta_{m,\widehat{m}}^{(1)} + \Delta_{m,\widehat{m}}^{(2)},$$

Using (8.7), we obtain

$$\frac{1}{3}\|\hat{f}_{\hat{m}} - f\|_2^2 \leq 3\|f_m - f\|_2^2 + \text{pen}(m) + \Delta_{m,\hat{m}}^{(1)} + \Delta_{m,\hat{m}}^{(2)}, \quad (8.11)$$

Now we have

$$\begin{aligned} \Delta_{m,\hat{m}}^{(2)} &= 6 \sup_{\substack{\mathbf{t} \in S_{\hat{m} \vee m} \\ \|\mathbf{t}\|=1}} \langle \mathbf{t}, \mathbf{G}_{m \vee \hat{m}}^{-1} J_{m \vee \hat{m}, M} (\Phi_M^T \Phi_M)^{-1} \Phi_M^T (\vec{q} - \vec{q}_M) \rangle^2 - \frac{1}{4} \text{pen}(\hat{m}) \\ &\leq 6 \|\mathbf{G}_{m \vee \hat{m}}^{-1} J_{m \vee \hat{m}, M} (\Phi_M^T \Phi_M)^{-1} \Phi_M^T (\vec{q} - \vec{q}_M)\|^2 - \frac{1}{4} \text{pen}(\hat{m}) \end{aligned}$$

and under **(A0)**, $M = n^{(1+\eta)/3}$ and $n \geq (2aC_q/\sigma^2)^{1/\eta}$, we get, as in (8.4),

$$\begin{aligned} 6 \|\mathbf{G}_{m \vee \hat{m}}^{-1} J_{m \vee \hat{m}, M} (\Phi_M^T \Phi_M)^{-1} \Phi_M^T (\vec{q} - \vec{q}_M)\|^2 &\leq 2 \frac{T}{n} \sigma^2 \text{Tr}(\mathbf{Q}_{m \vee \hat{m}}) \leq 2 \frac{T}{n} \sigma^2 (\text{Tr}(\mathbf{Q}_m) + \text{Tr}(\mathbf{Q}_{\hat{m}})) \\ &\leq \frac{1}{4} (\text{pen}(m) + \text{pen}(\hat{m})). \end{aligned}$$

As a consequence

$$\Delta_{m,\hat{m}}^{(2)} \leq \frac{1}{4} \text{pen}(m). \quad (8.12)$$

Now, denote

$$\tau(m, m') = 2 \frac{T}{n} [v_{m^*}^2 + \log((m^* \rho_{m^*}/\rho_1)^{2\kappa}) \rho_{m^*}^2], \quad (8.13)$$

where $m^* = m \vee m'$. Then

$$\Delta_{m,\hat{m}}^{(1)} \leq 3\sigma^2 \left[\sup_{\mathbf{t} \in S_{m \vee \hat{m}}} \langle \mathbf{t}, \mathbf{G}_M^{-1} (\Phi_M^T \Phi_M)^{-1} \Phi_M^T \vec{\varepsilon} \rangle^2 - \tau(m, \hat{m}) \right]_+ + 3\sigma^2 \tau(m, \hat{m}) - \frac{3}{4} \text{pen}(\hat{m}). \quad (8.14)$$

Using the fact that $3\sigma^2 \tau(m, \hat{m}) \leq (3/4)(\text{pen}(m) + \text{pen}(\hat{m}))$, combining (8.11), (8.12) and (8.14), we derive

$$\frac{1}{3}\|\hat{f}_{\hat{m}} - f\|_2^2 \leq 3\|f_m - f\|_2^2 + 2\text{pen}(m) + 3\sigma^2 \left[\sup_{\mathbf{t} \in S_{m \vee \hat{m}}} \langle \mathbf{t}, \mathbf{G}_M^{-1} (\Phi_M^T \Phi_M)^{-1} \Phi_M^T \vec{\varepsilon} \rangle^2 - \tau(m, \hat{m}) \right]_+,$$

We obtain

$$\begin{aligned} \|\hat{f}_{\hat{m}} - f\|_2^2 &\leq 9\|f_m - f\|_2^2 + 6\text{pen}(m) \\ &\quad + 9\sigma^2 \left[\sup_{\mathbf{t} \in S_{m \vee \hat{m}}} \langle \mathbf{t}, \mathbf{G}_M^{-1} (\Phi_M^T \Phi_M)^{-1} \Phi_M^T \vec{\varepsilon} \rangle^2 - \tau(m, \hat{m}) \right]_+. \end{aligned} \quad (8.15)$$

Hence, validity of Theorem 1 rests on the following lemma which will be proved later.

Lemma 2. *Under the assumptions of Theorem 1, for any $m \geq 1$, one has*

$$\mathbb{E} \left[\sup_{\mathbf{t} \in S_{m \vee \hat{m}}, \|\mathbf{t}\|=1} \langle \mathbf{t}, \mathbf{G}_M^{-1} (\Phi_M^T \Phi_M)^{-1} \Phi_M^T \vec{\varepsilon} \rangle^2 - \tau(m, \hat{m}) \right]_+ \leq \frac{8T\rho_1^2}{mn}.$$

Proof of Lemma 2 is given in Appendix A.3.

Proof of Theorem 2. Let $m_0 = \arg \min_m [\|f_m - f\|_2^2 + \sigma^2 T n^{-1} \log(m) v_m^2]$. Then, due to bounds (3.5) on v_m^2 , one has $m_0 \rightarrow \infty$ and $(m_0^{2r+1} T)/n \rightarrow 0$ as $T/n \rightarrow 0$. Hence, it also follows from (3.5)(see Lemma 4) that $\rho_m^2 \log(m^2 \rho_m^2) \propto \log(m) v_m^2$ as $m \rightarrow \infty$ which, in combination with Theorem 1, completes the proof.

References

- [1] Abramovich, F., Pensky, M., Rozenholc, Y. (2013). Laplace deconvolution with noisy observations. *Electronic Journal of Statistics* **7**, 1094-1128.
- [2] Abramovich, F., and Silverman, B.W. (1998). Wavelet decomposition approaches to statistical inverse problems. *Biometrika*, **85**, 115-129.
- [3] Abramowitz, M. and Stegun, I. A. (1964) Handbook of mathematical functions with formulas, graphs, and mathematical tables. *National Bureau of Standards Applied Mathematics Series*, 55, Washington, D.C.
- [4] Ameloot, M., Hendrickx, H. (1983) Extension of the performance of Laplace deconvolution in the analysis of fluorescence decay curves. *Biophys. Journ.*, **44**, 27 - 38.
- [5] Ameloot, M., Hendrickx, H., Herreman, W., Pottel, H., Van Cauwelaert, F., and van der Meer, W. (1984) Effect of orientational order on the decay of the fluorescence anisotropy in membrane suspensions. Experimental verification on unilamellar vesicles and lipid/alpha-lactalbumin complexes. *Biophys. Journ.*, **46**, 525 - 539.
- [6] Axel, L. (1980) Cerebral blood flow determination by rapid-sequence computed tomography: theoretical analysis. *Radiology*, **137**, 679-686.
- [7] Bongioanni, B., and Torrea, J. L. (2009) What is a Sobolev space for the Laguerre function systems? *Studia Math.* **192**, 147-172.
- [8] Böttcher, A., and Grudsky, S.M. (2000) Toeplitz Matrices, Asymptotic Linear Algebra, and Functional Analysis. *Birkhauser Verlag, Basel-Boston-Berlin*.
- [9] Böttcher, A., and Grudsky, S.M. (2005) Spectral Properties of Banded Toeplitz Matrices, *SIAM*, Philadelphia.
- [10] Cao Y. (2011) The promise of dynamic contrast-enhanced imaging in radiation therapy, *Semin Radiat Oncol.* **2**, 147-56.
- [11] Carroll, R. J., and Hall, P. (1988). Optimal rates of convergence for deconvolving a density. *J. Amer. Statist. Assoc.* **83**, 1184-1186.
- [12] Chauveau, D.E., van Rooij, A.C.M. and Ruymgaart, F.H. (1994). Regularized inversion of noisy Laplace transform. *Adv. Applied Math.* **15**, 186-201.
- [13] Cinzori, A.C., and Lamm, P.K. (2000) Future polynomial regularization of ill-posed Volterra equations. *SIAM J. Numer. Anal.*, **37**, 949-979.
- [14] Comte, F., Cuenod, C.A., Pensky, M., and Rozenholc, Y. (2012) Laplace deconvolution and its application to Dynamic Contrast Enhanced imaging. *ArXiv Preprint: 1207.2231.v1*
- [15] Comte, F., Rozenholc, Y., and Taupin, M.L. (2006) Penalized contrast estimator for density deconvolution. *The Canadian Journal of Statistics*, **34**, 431-452.
- [16] Delaigle, A., Hall, P. and Meister, A. (2008). On deconvolution with repeated measurements. *Ann. Statist.*, **36**, 665-685.

- [17] Dey, A.K., Martin, C.F. and Ruymgaart, F.H. (1998). Input recovery from noisy output data, using regularized inversion of Laplace transform. *IEEE Trans. Inform. Theory*, **44**, 1125–1130.
- [18] Diggle, P. J., and Hall, P. (1993). A Fourier approach to nonparametric deconvolution of a density estimate. *J. Roy. Statist. Soc. Ser. B*, **55** 523–531.
- [19] Fan, J. (1991). On the optimal rates of convergence for nonparametric deconvolution problem. *Ann. Statist.*, **19**, 1257–1272.
- [20] Fan, J. and Koo, J. (2002). Wavelet deconvolution. *IEEE Trans. Inform. Theory*, **48**, 734–747.
- [21] Fieselmann, A., Kowarschik, M., Ganguly, A., Hornegger, J., and Fahrig, R. (2011) Deconvolution-based CT and MR brain perfusion measurement: theoretical model revisited and practical implementation details. *Int. J. Biomed. Imaging*, **2011**, 467–563.
- [22] Gafni, A., Modlin, R. L. and Brand, L. (1975) Analysis of fluorescence decay curves by means of the Laplace transformation. *Biophys. J.*, **15**, 263–280.
- [23] Gendre, X. (2014). Model selection and estimation of a component in additive regression. To appear in *ESAIM Probab. Stat.* **18**, 77–116.
- [24] Gripenberg, G., Londen, S.O., and Staffans, O. (1990) *Volterra Integral and Functional Equations*. Cambridge University Press, Cambridge.
- [25] Gohberg, I.C., Feldman, I.A. (1974) *Convolution equations and projection methods for their solution*. Amer. Math. Soc., Providence.
- [26] Gradshteyn, I.S., Ryzhik, I.M. (1980) *Tables of integrals, series, and products*. Academic Press, New York.
- [27] Johnstone, I.M., Kerkycharian, G., Picard, D. and Raimondo, M. (2004) Wavelet deconvolution in a periodic setting. *J. Roy. Statist. Soc. Ser. B*, **66**, 547–573.
- [28] Lakowicz, J.R. (2006) *Principles of Fluorescence Spectroscopy*. Kluwer Academic, New York.
- [29] Lamm, P. (1996) Approximation of ill-posed Volterra problems via predictor-corrector regularization methods. *SIAM J. Appl. Math.*, **56**, 524–541.
- [30] Laurent, B., Massart, P. B. (2000). Adaptive estimation of a quadratic functional by model selection. *Ann. Statist.*, **28**, 1302–1338.
- [31] Lien, T.N., Trong, D.D. and Dinh, A.P.N. (2008) Laguerre polynomials and the inverse Laplace transform using discrete data *J. Math. Anal. Appl.*, **337**, 1302–1314.
- [32] Lieury, T., Pouzat, C. and Rozenholc, Y. (2012) DynClust: non-parametric denoising and clustering method of noisy images both indexed by time and space, *R-package* available at <http://cran.r-project.org/>.
- [33] Maleknejad, K., Mollapourasl, R. and Alizadeh, M. (2007) Numerical solution of Volterra type integral equation of the first kind with wavelet basis. *Appl. Math. Comput.*, **194**, 400–405.
- [34] Mnatsakanov, R.M. (2011). Moment-recovered approximations of multivariate distributions: The Laplace transform inversion. *Statist. Probab. Lett.*, **81**, 1–7.

- [35] Mnatsakanov, R.M. and Sarkisian, K. (2013). A note on recovering the distributions from exponential moments. *Applied Mathematics and Computation*. **219**, 8730–8737.
- [36] O'Connor, D. V., Ware, W. R. and Andre, J. C. (1979) Deconvolution of fluorescence decay curves. A critical comparison of techniques. *J. Phys. Chem.*, **83**, 1333-1343.
- [37] Ostergaard, L., Weisskoff, R.M., Chesler, D.A., Gyldensted, C., and Rosen, B.R. (1996) High resolution measurement of cerebral blood flow using intravascular tracer bolus passages. Part I: Mathematical approach and statistical analysis. *Magn. Reson. Med.*, **36**, 715–725.
- [38] Pensky, M., and Vidakovic, B. (1999). Adaptive wavelet estimator for nonparametric density deconvolution. *Ann. Statist.*, **27**, 2033–2053.
- [39] Polyanin, A.D., and Manzhirov, A.V. (1998) *Handbook of Integral Equations*, CRC Press, Boca Raton, Florida.
- [40] REMISCAN - Project number IDRCB 2007-A00518-45/P060407/STIC 2006; Research Ethics Board (REB) approved- cohort funding by INCa (1M Euros) and promoted by the AP-HP (Assistance Publique Hôpitaux de Paris). Inclusion target: 100 patients. Ongoing since 2007.
- [41] Rozenholc, Y., and Reiß, M. (2012) Preserving time structures while denoising a dynamical image, *Mathematical Methods for Signal and Image Analysis and Representation (Chapter 12)*, Florack, L. and Duits, R. and Jongbloed, G. and van Lieshout, M.-C. and Davies, L. Ed., Springer-Verlag, Berlin.
- [42] Rozenholc, Y. , Reiß, M., Balvay, D. and Cuenod, C.-A. (2010) Growing time-homogeneous neighborhoods for denoising and clustering Dynamic Contrast Enhanced-CT sequences, *Preprint*: <http://hal.archives-ouvertes.fr/hal-00712348/>.
- [43] Rudelson, M. and Vershynin, R. (2013) Hanson-Wright inequality and sub-Gaussian concentration. *Electron. Commun. Probab.* **18**, paper 82, 9 pp.
- [44] Stefanski, L., and Carroll, R. J. (1990). Deconvoluting kernel density estimators. *Statistics*, **21**, 169-184.
- [45] Vareschi T. (2013) Noisy Laplace deconvolution with error in the operator. *ArXiv Preprint*: 1303.7437.v2. Journal of Statistical Planning and Inference Volumes 157158, FebruaryMarch 2015, Pages 16-35
- [46] Vershynin, R. (2012) Introduction to the non-asymptotic analysis of random matrices. Chapter 5 in *Compressed sensing. Theory and applications*. Edited by Y.C. Eldar and G. Kutyniok. Cambridge University Press, Cambridge, 210-268.
- [47] Weeks, W.T. (1966) Numerical Inversion of Laplace Transforms Using Laguerre Functions. *J. Assoc. Comput. Machinery*, **13**, 419 - 429.

Fabienne Comte
 Sorbonne Paris Cité
 Université Paris Descartes,
 MAP5, UMR CNRS 8145, France
fabienne.comte@parisdescartes.fr

Charles-André Cuenod
Sorbonne Paris Cité
Université Paris Descartes, PARCC
European Hospital George Pompidou (HEGP-APHP)
LRI, INSERM U970-PARCC, France
ca@cuenod.net

Marianna Pensky
Department of Mathematics
University of Central Florida
Orlando FL 32816-1353, USA
marianna.pensky@ucf.edu

Yves Rozenholc
Sorbonne Paris Cité
Université Paris Descartes,
MAP5, UMR CNRS 8145, France
yves.rozenholc@parisdescartes.fr

A Supplementary materials

A.1 Introduction to theory of banded Toeplitz matrices

The proof of asymptotic optimality of the estimator $\hat{f}_{\hat{m}}$ relies heavily on the theory of banded Toeplitz matrices developed in Böttcher and Grudsky (2000, 2005). In this subsection, we review some of the facts about Toeplitz matrices which we shall use later.

Consider a sequence of numbers $\{b_k\}_{k=-\infty}^{\infty}$ such that $\sum_{k=-\infty}^{\infty} |b_k| < \infty$. An infinite Toeplitz matrix $T = T(b)$ is the matrix with elements $T_{i,j} = b_{i-j}$, $i, j = 0, 1, \dots$.

Let $\mathcal{C} = \{z \in \mathbb{C} : |z| = 1\}$ be the complex unit circle. With each Toeplitz matrix $T(b)$ we can associate its symbol

$$b(z) = \sum_{k=-\infty}^{\infty} b_k z^k, \quad z \in \mathcal{C}. \quad (\text{A.1})$$

Since, $B(\theta) = b(e^{i\theta}) = \sum_{k=-\infty}^{\infty} b_k e^{ik\theta}$, numbers b_k are Fourier coefficients of function $B(\theta) = b(e^{i\theta})$.

There is a very strong link between properties of a Toeplitz matrix $T(b)$ and function $b(z)$. In particular, if $b(z) \neq 0$ for $z \in \mathcal{C}$ and $\text{wind}(b) = J_b$, then $b(z)$ allows Wiener-Hopf factorization $b(z) = b_-(z) b_+(z) z^{J_b}$ where b_+ and b_- have the following forms

$$b_-(z) = \sum_{k=0}^{\infty} b_{-k}^- z^{-k}, \quad b_+(z) = \sum_{k=0}^{\infty} b_k^+ z^k$$

(see Theorem 1.8 of Böttcher and Grudsky (2005)).

If $T(b)$ is a lower triangular Toeplitz matrix, then $b(z) \equiv b_+(z)$ with $b_k^+ = b_k$. In this case, the product of two Toeplitz matrices can be obtained by simply multiplying their symbols and the inverse of a Toeplitz matrix can be obtained by taking the reciprocal of function $b_+(z)$:

$$T(b_+ d_+) = T(b_+) T(d_+), \quad T^{-1}(b_+) = T(1/b_+). \quad (\text{A.2})$$

Let $T_m(b) = T_m(b_+) \in R^{m \times m}$ be a banded lower triangular Toeplitz matrix corresponding to the Laurent polynomial $b(z) = \sum_{k=0}^{m-1} b_k z^k$.

In practice, one usually use only finite, banded, Toeplitz matrices with elements $T_{i,j}$, $i, j = 0, 1, \dots, m-1$. In this case, only a finite number of coefficients b_k do not vanish and function $b(z)$

in (A.1) reduces to a Laurent polynomial $b(z) = \sum_{k=-J}^K b_k z^k$, $z \in \mathcal{C}$, where J and K are nonnegative integers, $b_{-J} \neq 0$ and $b_K \neq 0$. If $b(z) \neq 0$ for $z \in \mathcal{C}$, then $b(z)$ can be represented in a form

$$b(z) = z^{-J} b_K \prod_{j=1}^{J_0} (z - \mu_j) \prod_{k=1}^{K_0} (z - \nu_k) \quad \text{with} \quad |\mu_j| < 1, |\nu_k| > 1. \quad (\text{A.3})$$

In this case, the winding number of $b(z)$ is $\text{wind}(b) = J_0 - J$.

Let $T_m(b) = T_m(b_+) \in R^{m \times m}$ be a banded lower triangular Toeplitz matrix corresponding to the Laurent polynomial $b(z) = \sum_{k=0}^{m-1} b_k z^k$. If b has no zeros on the complex unit circle \mathcal{C} and

$\text{wind}(b) = 0$, then, due to Theorem 3.7 of Böttcher and Grudsky (2005), $T(b)$ is invertible and $\lim_{m \rightarrow \infty} \sup \rho(T_m^{-1}(b)) < \infty$. Moreover, by Corollary 3.8,

$$\lim_{m \rightarrow \infty} \rho(T_m^{-1}(b)) = \rho(T^{-1}(b)) \quad (\text{A.4})$$

A.2 Relation between ρ_m^2 and v_m^2

In order to apply the theory surveyed above, we first need to examine function $b(z)$ associated with the infinite lower triangular Toeplitz matrix \mathbf{G} defined in Lemma 1 the Laurent polynomial associated with its banded version \mathbf{G}_m . It turns out that $b(z)$ can be expressed via the Laplace transform $G(s)$ of the kernel $g(t)$. In particular, the following statement holds.

Lemma 3. *Consider a sequence $\{b_k\}_{k=0}^\infty$ with elements $b_0 = g^{(0)}$ and $b_k = g^{(k)} - g^{(k-1)}$, $k = 1, 2, \dots$ where $g^{(k)}$ are Laguerre coefficients of the kernel g in (1.1). Then, b_k , $k \geq 0$, are Fourier coefficients of the function*

$$b(e^{i\theta}) = G\left(\frac{a(1+e^{i\theta})}{(1-e^{i\theta})}\right) = \sum_{k=0}^{\infty} b_k e^{i\theta k}, \quad (\text{A.5})$$

where $G(s)$ is the Laplace transform of the kernel $g(x)$.

Proof. To prove this statement, we shall follow the theory of Wiener-Hopf integral equations described in Gohberg and Feldman (1974). Denote Fourier transform of a function $p(x)$ by $\hat{p}(\omega) = \int_{-\infty}^{\infty} e^{i\omega x} p(x) dx$ and observe that

$$\hat{\phi}_k(\omega) = (-1)^k \sqrt{2a} \frac{(a+i\omega)^k}{(a-i\omega)^{k+1}}.$$

Therefore, elements of the infinite Toeplitz matrix \mathbf{G} in Lemma 1 are generated by the sequence b_j , $j \geq 0$, where

$$\begin{aligned} b_j &= (2a)^{-1/2} (g^{(j)} - g^{(j-1)}) = \frac{1}{2\pi} \int_{-\infty}^{\infty} \hat{g}(\omega) [\overline{\hat{\phi}_j(\omega)} - \overline{\hat{\phi}_{j-1}(\omega)}] d\omega \\ &= \frac{a}{\pi} \int_{-\infty}^{\infty} \hat{g}(\omega) \left(\frac{i\omega - a}{i\omega + a} \right)^j \frac{d\omega}{a^2 + \omega^2}, \quad j = 0, 1, \dots \end{aligned} \quad (\text{A.6})$$

Note that $|(i\omega - a)/(i\omega + a)| = 1$, so that we can use the following substitution in the integral (A.6):

$$\frac{i\omega - a}{i\omega + a} = e^{-i\theta} \implies \omega = \frac{a(e^{i\theta} + 1)}{i(e^{i\theta} - 1)} = \frac{a \sin \theta}{\cos \theta - 1}, \quad 0 \leq \theta \leq 2\pi.$$

Simple calculations show that

$$b_j = \frac{1}{2\pi} \int_0^{2\pi} \hat{g}\left(\frac{a(e^{i\theta} + 1)}{i(e^{i\theta} - 1)}\right) e^{-i\theta j} d\theta,$$

so that b_j , $j \in \mathbb{Z}$, are Fourier coefficients of the function

$$B(\theta) = b(e^{i\theta}) = \hat{g}\left(\frac{a(e^{i\theta} + 1)}{i(e^{i\theta} - 1)}\right).$$

Now, let us show that $b_j = 0$ for $j < 0$. Indeed, if $j = -k$, $k > 0$, then

$$\begin{aligned} b_j &= \frac{a}{\pi} \int_{-\infty}^{\infty} \hat{g}(\omega) \left(\frac{i\omega + a}{i\omega - a} \right)^k \frac{d\omega}{a^2 + \omega^2} = \frac{a}{\pi} \int_{-\infty}^{\infty} \hat{g}(\omega) \left(\frac{i(-\omega) - a}{i(-\omega) + a} \right)^k \frac{d\omega}{a^2 + \omega^2} \\ &= \frac{1}{2\pi} \int_{-\infty}^{\infty} \hat{g}(\omega) [\hat{\phi}_j(-\omega) - \hat{\phi}_{j-1}(-\omega)] d\omega = \int_{-\infty}^{\infty} g(x) [\phi_j(-x) - \phi_{j-1}(-x)] dx = 0 \end{aligned}$$

since $g(x) = 0$ if $x < 0$ and $\phi_k(-x) = 0$ if $x > 0$. Hence, function $B(\theta) = b(e^{i\theta})$ has only coefficients b_j , $j \geq 0$, in its Fourier series. Now, to complete the proof, one just needs to note that $G(s) = \hat{g}(is)$ for any s such that Laplace transform $G(s)$ of g exists.

For any function $w(z)$ with an argument on a unit circle \mathcal{C} denote

$$\|w\|_{\text{circ}} = \max_{|z|=1} w(z).$$

The following lemma 4 shows that indeed $\rho_m^2 \log m = o(v_m^2)$ as $m \rightarrow \infty$.

Lemma 4. *Let $b(z)$ be given by (A.5), i.e., $b(z) = G(a(1+z)/(1-z))$, $|z| = 1$. Denote*

$$w(z) = (1-z)^{-r} b(z), \quad w^{-1}(z) = (1-z)^r b^{-1}(z), \quad |z| = 1. \quad (\text{A.7})$$

Then, under assumptions (A1)–(A3), $w(z)$ and $w^{-1}(z)$ have no zero on the complex unit circle and, for m large enough, one has

$$\frac{\lambda_1}{2(r!)^2} (\|w\|_{\text{circ}})^{-2} m^{2r} \leq \rho_m^2 \leq v_m^2 \leq 2\lambda_2 \|w^{-1}\|_{\text{circ}}^2 m^{2r}, \quad (\text{A.8})$$

where ρ_m^2 and v_m^2 are defined in (2.14), λ_1 and λ_2 are given by (3.3).

Proof of Lemma 4. Let us first find upper and lower bounds on $\|\mathbf{G}_m^{-1}\|_2^2 = \text{Tr}(\mathbf{G}_m^{-T} \mathbf{G}_m^{-1})$ and $\|\mathbf{G}_m^{-1}\|^2 = \lambda_{\max}(\mathbf{G}_m^{-T} \mathbf{G}_m^{-1})$. For this purpose, examine the function

$$b(z) = \hat{g} \left(\frac{a(z+1)}{i(z-1)} \right) = G \left(\frac{a(z+1)}{1-z} \right), \quad |z| = 1.$$

Denote $y = a(z+1)/(1-z)$, so that $z = (y-a)/(y+a)$ and $G(y) = b((y-a)/(y+a))$.

Let us show that, under Assumptions (A1)–(A3), $b(z)$ has a zero of order r at $z = 1$ and all other zeros of $b(z)$ lie outside the unit circle.

For this purpose, assume that $y = \alpha + i\beta$ is a zero of G , i.e. $G(\alpha + i\beta) = 0$. Simple calculus yields

$$\left| \frac{y-a}{y+a} \right|^2 = 1 - \frac{4\alpha a}{(\alpha+a)^2 + \beta^2},$$

so that $|z| = |(y-a)/(y+a)| \leq 1$ iff $\alpha \geq 0$. But, by Assumption (A2), $G(y)$ has no zeros with nonnegative real parts, so that $\alpha < 0$ and $|z| = |(y-a)/(y+a)| > 1$. Therefore, all zeros of $b(z)$, which correspond to finite zeros of G , lie outside the complex unit circle \mathcal{C} .

Assumptions (A1), (A2) and properties of Laplace transform imply that $G(s) = s^{-r}(B_r + G_r(s))$ where $G_r(s)$ is the Laplace transform of $g^{(r)}(t)$. Hence,

$$\lim_{\text{Re } s \rightarrow \infty} s^j G(s) = \begin{cases} 0, & \text{if } j = 0, \dots, r-1, \\ B_r \neq 0, & \text{if } j = r, \end{cases}$$

so that $y = \infty + i\beta$ is zero of order r of $G(y)$. Since $\lim_{Re\ y \rightarrow \infty} (y - a)/(y + a) = 1$, $b(z)$ has zero of order r at $z = 1$.

Then, $b(z)$ can be written as $b(z) = (1 - z)^r w(z)$ where $w(z)$ is defined by formula (A.7) and all zeros of $w(z)$ lie outside the complex unit circle. Therefore, $w(z)$ can be written as

$$w(z) = C_w \prod_{j=1}^N (z - \zeta_j), \quad 0 \leq N \leq \infty, \quad |\zeta_j| > 1, \quad (\text{A.9})$$

where C_w is an absolute constant. Since $b(z)$ does not contain any negative powers of z in its representation, $J_0 = 0$ and $J = 0$ in (A.3) and, consequently, $\text{wind}(w) = 0$. Also, by (A.2) and (A.7), one has $T^{-1}(b) = T(b^{-1})$ where $b^{-1}(z) = w^{-1}(z)(1 - z)^{-r}$.

Now, recall that $\|\mathbf{G}_m^{-1}\|_2^2 = \|T_m(b^{-1})\|_2^2$ and $\rho^2(\mathbf{G}_m^{-1}) = \rho^2(T_m(b^{-1}))$. Using relation between Frobenius and spectral norms $\|\mathbf{A}_1 \mathbf{A}_2\|_2 \leq \|\mathbf{A}_1\|_2 \rho(\mathbf{A}_2)$ for any matrices \mathbf{A}_1 and \mathbf{A}_2 (see, e.g., Böttcher and Grudsky (2000), page 116), obtain

$$\|T_m(b^{-1})\|_2 \leq \|T_m((1 - z)^{-r})\|_2 \rho(T_m(w^{-1})), \quad \rho(T_m(b^{-1})) \leq \rho(T_m((1 - z)^{-r})) \rho(T_m(w^{-1})), \quad (\text{A.10})$$

$$\|T_m((1 - z)^{-r})\|_2 \leq \|T_m(b^{-1})\|_2 \rho(T_m(w)), \quad \rho(T_m((1 - z)^{-r})) \leq \rho(T_m(b^{-1})) \rho(T_m(w)). \quad (\text{A.11})$$

Note that (see Böttcher and Grudsky (2005), page 13)

$$\lim_{m \rightarrow \infty} \rho(T_m(w^{-1})) = \|w^{-1}\|_{\text{circ}}, \quad \lim_{m \rightarrow \infty} \rho(T_m(w)) = \|w\|_{\text{circ}},$$

Also, due to representation (A.9), both w and w^{-1} are bounded, and, therefore, $0 < \|w^{-1}\|_{\text{circ}} < \infty$ and $0 < \|w\|_{\text{circ}} < \infty$. Denote

$$\nu_f(m) = \|T_m((1 - z)^{-r})\|_2, \quad \nu_s(m) = \rho(T_m((1 - z)^{-r})). \quad (\text{A.12})$$

Then, it follows from (A.4), (A.10) and (A.11) that, for m large enough,

$$0.5 (\|w\|_{\text{circ}})^{-2} \nu_f^2(m) \leq \|T_m(b^{-1})\|_2^2 \leq 2 \|w^{-1}\|_{\text{circ}}^2 \nu_f^2(m), \quad (\text{A.13})$$

$$0.5 (\|w\|_{\text{circ}})^{-2} \nu_s^2(m) \leq \rho^2(T_m(b^{-1})) \leq 2 \|w^{-1}\|_{\text{circ}}^2 \nu_s^2(m). \quad (\text{A.14})$$

In order to finish the proof, we need to evaluate $\nu_f^2(m)$ and $\nu_s^2(m)$ and also to derive a relation between v_m^2 , ρ_m^2 , $\|T_m(b^{-1})\|_2^2$ and $\rho^2(T_m(b^{-1}))$. The first task is accomplished by the following lemma.

Lemma 5. *Let $\nu_f(m)$ and $\nu_s(m)$ be defined in (A.12). Then,*

$$\nu_f^2(m) \leq m^{2r}, \quad (\text{A.15})$$

$$(r!)^{-2} m^{2r} \leq \nu_s^2(m). \quad (\text{A.16})$$

Proof of Lemma 5 is given in Section A.3.

Now, to complete the proof, note that due to relation between Frobenius and spectral norms

$$\begin{aligned} v_m^2 &= \text{Tr}(\mathbf{\Omega}_m \mathbf{G}_m^{-T} \mathbf{G}_m^{-1}) \leq \lambda_2 \|\mathbf{G}_m^{-1}\|_2^2 = \lambda_2 \|T_m(b^{-1})\|_2^2, \\ \rho^2(T_m(b^{-1})) &= \lambda_{\max}(\mathbf{G}_m^{-T} \mathbf{G}_m^{-1}) \leq \lambda_1^{-1} \rho_m^2, \end{aligned}$$

so that

$$\rho_m^2 \geq \lambda_1 \rho^2(T_m(b^{-1})), \quad v_m^2 \leq \lambda_2 \|T_m(b^{-1})\|_2^2. \quad (\text{A.17})$$

Combination of (A.13) – (A.17) and Lemma 5 complete the proof.

A.3 Proofs of supplementary Lemmas

Proof of Lemma 2.

The proof of Lemma 2 has two steps. The first one is the application of a χ^2 -type deviation inequality. The second step consists of integrating this deviation inequality.

The χ^2 -inequality is formulated as follows. In the Gaussian case, it is stated in Laurent and Massart (2000), and improved by Gendre (see Lemma 8.2 of Gendre (2009)). In the sub-Gaussian case, it is given in Rudelson and Vershynin (2013), Theorem 2.1. Let \mathbf{A} be a $p \times p$ matrix $\mathbf{A} \in \mathbb{M}_p(\mathbb{R})$ and $\boldsymbol{\zeta}$ be a vector of sub-Gaussian random variables. Then, for any $x > 0$,

$$\mathbb{P} \left(\|\mathbf{A}\boldsymbol{\zeta}\|^2 \geq \|\mathbf{A}\|_2^2 + 2\sqrt{\|\mathbf{A}\|_2^2 \rho^2(\mathbf{A})x} + \rho^2(\mathbf{A})x \right) \leq 2e^{-x/\kappa}. \quad (\text{A.18})$$

In the Gaussian case, namely, for $\boldsymbol{\zeta}$ a standard Gaussian vector, we have $\kappa = 1$.

Now, recall that for $\mathbf{t} \in S_m + S_{m'} = S_{m^*}$ where $m^* = m \vee m'$, one has

$$\langle \mathbf{t}, \mathbf{G}_M^{-1}(\Phi_M^T \Phi_M)^{-1} \Phi_M^T \bar{\boldsymbol{\varepsilon}} \rangle = \sqrt{\frac{T}{n}} \langle [\mathbf{t}]_{m^*}, \mathbf{A}_{m^*} \bar{\boldsymbol{\varepsilon}} \rangle$$

where we recall that $[\mathbf{t}]_{m^*}$ is the m^* -dimensional vector formed by the first m^* coordinates of \mathbf{t} and \mathbf{A}_{m^*} is defined by (2.13). Moreover,

$$\sup_{\mathbf{t} \in S_m + S_{m'}, \|\mathbf{t}\|=1} \langle \mathbf{t}, \mathbf{G}_M^{-1}(\Phi_M^T \Phi_M)^{-1} \Phi_M^T \bar{\boldsymbol{\varepsilon}} \rangle^2 = \frac{T}{n} \|\mathbf{A}_{m^*} \bar{\boldsymbol{\varepsilon}}\|^2.$$

Thus, it follows from (A.18) that

$$\mathbb{P} \left(\|\mathbf{A}_{m^*} \bar{\boldsymbol{\varepsilon}}\|^2 \geq v_{m^*}^2 + 2\sqrt{\rho_{m^*}^2 v_{m^*}^2 x} + \rho_{m^*}^2 x \right) \leq 2e^{-x/\kappa}. \quad (\text{A.19})$$

One has $2\sqrt{\rho_{m^*}^2 v_{m^*}^2 x} \leq v_{m^*}^2 + \rho_{m^*}^2 x$ so that

$$\mathbb{P} (\|\mathbf{A}_{m^*} \bar{\boldsymbol{\varepsilon}}\|^2 \geq 2v_{m^*}^2 + 2\rho_{m^*}^2 x) \leq 2e^{-x/\kappa}.$$

Therefore, using definition (8.13) of $\tau(m, m')$, obtain

$$\begin{aligned} & \mathbb{E} \left(\sup_{\mathbf{t} \in S_m + S_{m'}, \|\mathbf{t}\|=1} \langle \mathbf{t}, \mathbf{G}_M^{-1}(\Phi_M^T \Phi_M)^{-1} \Phi_M^T \bar{\boldsymbol{\varepsilon}} \rangle^2 - \tau(m, m') \right)_+ = \mathbb{E} \left(\frac{T}{n} \|\mathbf{A}_{m^*} \bar{\boldsymbol{\varepsilon}}\|^2 - \tau(m, m') \right)_+ \\ & \leq \frac{T}{n} \int_0^{+\infty} \mathbb{P} (\|\mathbf{A}_{m^*} \bar{\boldsymbol{\varepsilon}}\|^2 - [2v_{m^*}^2 + 2\log[(m^* \rho_{m^*}/\rho_1)^{2\kappa}] \rho_{m^*}^2] \geq \xi) d\xi. \end{aligned}$$

Changing variables

$$2\log[(m^* \rho_{m^*}/\rho_1)^{2\kappa}] \rho_{m^*}^2 + \xi = 2\rho_{m^*}^2 x$$

and application of (A.19) yield

$$\begin{aligned} \mathbb{E} \left(\sup_{\mathbf{t} \in S_m + S_{m'}, \|\mathbf{t}\|=1} \langle \mathbf{t}, \mathbf{G}_M^{-1} \Phi_M^T \Phi_M)^{-1} \Phi_M^T \bar{\boldsymbol{\varepsilon}} \rangle^2 - \tau(m, m') \right)_+ & \leq 4 \frac{T}{n} \rho_{m^*}^2 \int_{\log[(m^* \rho_{m^*}/\rho_1)^{2\kappa}] }^{+\infty} e^{-x/\kappa} dx \\ & = 4 \frac{T}{n} \rho_1^2 (m^*)^{-2}. \end{aligned}$$

Thus we obtain

$$\begin{aligned} & \mathbb{E} \left[\sup_{\mathbf{t} \in S_m \vee \widehat{m}} \langle \mathbf{t}, \mathbf{G}_M^{-1} \Phi_M^T \Phi_M \rangle^{-1} \Phi_M^T \tilde{\varepsilon} \rangle^2 - \tau(m, \widehat{m}) \right]_+ \\ & \leq \sum_{m' \in \mathcal{M}_n} \mathbb{E} \left(\sup_{\mathbf{t} \in S_m + S_{m'}, \|\mathbf{t}\|=1} \langle \mathbf{t}, \mathbf{G}_M^{-1} \Phi_M^T \Phi_M \rangle^{-1} \Phi_M^T \tilde{\varepsilon} \rangle^2 - \tau(m, m') \right)_+ \end{aligned}$$

and

$$\begin{aligned} & \sum_{m' \in \mathcal{M}_n} \mathbb{E} \left(\sup_{\mathbf{t} \in S_m + S_{m'}, \|\mathbf{t}\|=1} \langle \mathbf{t}, \mathbf{G}_M^{-1} \Phi_M^T \Phi_M \rangle^{-1} \Phi_M^T \tilde{\varepsilon} \rangle^2 - \tau(m, m') \right)_+ \\ & \leq 4\rho_1^2 \frac{T}{n} \sum_{m' \in \mathcal{M}_n} (m \vee m')^{-2} \\ & \leq 4\rho_1^2 \frac{T}{n} \left(\sum_{m'=1}^m m^{-2} + \sum_{m'>m} (m')^{-2} \right) \\ & \leq 4\rho_1^2 \frac{T}{n} \left(m^{-1} + \int_m^{+\infty} \frac{dx}{x^2} \right) = 8\rho_1^2 \frac{T}{nm}, \end{aligned}$$

which concludes the proof. \square

Proof of Lemma 5. Note that, by formula 1.110 of Gradshteyn and Ryzhik (1980),

$$(1-z)^{-r} = \sum_{j=0}^{\infty} \binom{r+j-1}{j} z^j,$$

so that, by definition of Frobenius norm,

$$\begin{aligned} \|T_m((1-z)^{-r})\|_2^2 &= m + (m-1) \binom{r}{1}^2 + (m-2) \binom{r+1}{2}^2 + \dots + \binom{r+m-2}{m-1}^2 \\ &= \sum_{j=0}^{m-1} \binom{r+j-1}{j}^2 (m-j), \\ \rho(T_m((1-z)^{-r})) &= \max_{|z|=1} \left| \sum_{j=0}^{m-1} \binom{r+j-1}{j} z^j \right| = \sum_{j=0}^{m-1} \binom{r+j-1}{r-1}. \end{aligned}$$

If $r = 1$, then

$$\sum_{j=0}^{m-1} \binom{r+j-1}{j}^2 (m-j) = \sum_{j=0}^{m-1} (m-j) = \frac{m(m+1)}{2}.$$

If $r \geq 2$, then

$$\frac{j^{r-1}}{(r-1)!} \leq \binom{r+j-1}{j} = \frac{(r-1+1) \dots (r-1+j)}{(r-1)!} \leq (j+1)^{r-1},$$

so that, for $m \geq 4$,

$$\nu_f^2(m) = \|T_m((1-z)^{-r})\|_2^2 \leq m^{2r},$$

which proves validity of (A.15). To show that (A.16) holds, observe that, by formula 0.151.1 of Gradshtein and Ryzhik (1980),

$$\sum_{j=0}^{m-1} \binom{r+j-1}{r-1} = \binom{r+m-1}{r}, \quad \frac{m^r}{r!} \leq \binom{r+m-1}{r} \leq m^r.$$

B Simulation tables

Table 1 provides the averages and their standard deviations (in *italic*) of the $ISE(\hat{f}_{\text{LAG}})$ computed over 400 simulation runs.

		g_1		g_2		g_3		g_4		g_5	
n		100	250	100	250	100	250	100	250	100	250
f_1	$i = 1$	173	39.9	5.50	2.33	31.8	11.9	182	123	201	175
		<i>50.4</i>	<i>52.4</i>	<i>7.07</i>	<i>2.50</i>	<i>46.9</i>	<i>13.0</i>	<i>50.9</i>	<i>67.3</i>	<i>80.4</i>	<i>52.4</i>
	$i = 2$	21.7	14.9	1.35	0.69	7.94	3.35	35.4	12.7	110	20.5
		<i>30.5</i>	<i>9.02</i>	<i>2.07</i>	<i>0.87</i>	<i>11.7</i>	<i>6.30</i>	<i>54.1</i>	<i>14.3</i>	<i>80.0</i>	<i>24.3</i>
	$i = 3$	6.18	10.1	0.65	0.35	2.18	0.87	8.42	9.89	13.6	10.6
		<i>9.22</i>	<i>6.91</i>	<i>0.87</i>	<i>0.29</i>	<i>4.91</i>	<i>1.54</i>	<i>12.4</i>	<i>9.86</i>	<i>20.1</i>	<i>6.88</i>
	$i = 4$	10.9	5.15	0.14	0.089	0.60	0.28	1.99	6.20	4.93	22.2
		<i>5.63</i>	<i>4.23</i>	<i>0.13</i>	<i>0.080</i>	<i>1.01</i>	<i>0.64</i>	<i>3.36</i>	<i>4.29</i>	<i>14.0</i>	<i>27.6</i>
	$i = 5$	2.05	1.67	0.050	0.048	0.24	0.095	3.27	2.16	10.8	4.79
		<i>2.01</i>	<i>0.50</i>	<i>0.033</i>	<i>0.043</i>	<i>0.55</i>	<i>0.18</i>	<i>9.72</i>	<i>2.77</i>	<i>10.7</i>	<i>3.39</i>
f_2	$i = 1$	252	62.7	20.7	20.5	7.18	3.34	896	215	144	389
		<i>65.2</i>	<i>42.0</i>	<i>8.79</i>	<i>7.07</i>	<i>14.0</i>	<i>4.59</i>	<i>637</i>	<i>148</i>	<i>290</i>	<i>115</i>
	$i = 2$	194	20.1	10.5	13.3	1.77	0.77	871	321	285	29.0
		<i>239</i>	<i>14.3</i>	<i>6.07</i>	<i>3.83</i>	<i>5.11</i>	<i>1.19</i>	<i>685</i>	<i>174</i>	<i>202</i>	<i>12.5</i>
	$i = 3$	160	17.3	5.75	8.3	0.46	0.20	149	252	179	34.5
		<i>37</i>	<i>4.39</i>	<i>3.22</i>	<i>3.69</i>	<i>1.37</i>	<i>0.30</i>	<i>176</i>	<i>72.8</i>	<i>53.6</i>	<i>98.8</i>
	$i = 4$	227	73.6	3.47	3.5	0.14	0.056	111	12.5	242	59.1
		<i>26.6</i>	<i>74.4</i>	<i>2.91</i>	<i>1.7</i>	<i>0.54</i>	<i>0.065</i>	<i>39.2</i>	<i>64.5</i>	<i>127</i>	<i>73.3</i>
	$i = 5$	257	44.7	2.35	1.59	0.23	0.019	218	62	224	51.4
		<i>41.4</i>	<i>31.5</i>	<i>3.93</i>	<i>0.39</i>	<i>0.65</i>	<i>0.023</i>	<i>82.1</i>	<i>74.3</i>	<i>61.8</i>	<i>19.5</i>
f_3	$i = 1$	46.1	22.2	5.33	2.59	27.9	23.0	72.2	31.7	165	45.2
		<i>51.3</i>	<i>13.3</i>	<i>5.19</i>	<i>3.03</i>	<i>26.3</i>	<i>23.3</i>	<i>106</i>	<i>25.9</i>	<i>238</i>	<i>43.1</i>
	$i = 2$	21.2	13.0	1.46	0.77	16.2	5.09	27.3	16.7	45.2	20.4
		<i>15.8</i>	<i>3.15</i>	<i>1.55</i>	<i>0.82</i>	<i>16.5</i>	<i>6.04</i>	<i>27.0</i>	<i>8.49</i>	<i>57.4</i>	<i>12.3</i>
	$i = 3$	14.0	5.60	0.46	0.21	3.77	1.43	18.1	7.64	23.5	16.3
		<i>5.78</i>	<i>7.02</i>	<i>0.36</i>	<i>0.20</i>	<i>5.01</i>	<i>1.75</i>	<i>11.8</i>	<i>8.24</i>	<i>24.4</i>	<i>10.1</i>
	$i = 4$	9.94	2.01	0.108	0.056	1.00	0.55	4.89	1.76	14.6	2.85
		<i>8.68</i>	<i>2.50</i>	<i>0.14</i>	<i>0.055</i>	<i>1.33</i>	<i>0.61</i>	<i>7.03</i>	<i>2.10</i>	<i>13.7</i>	<i>3.38</i>
	$i = 5$	7.62	1.00	0.025	0.015	0.50	0.17	2.50	0.51	7.70	0.75
		<i>3.39</i>	<i>0.89</i>	<i>0.019</i>	<i>0.018</i>	<i>0.56</i>	<i>0.149</i>	<i>2.81</i>	<i>0.46</i>	<i>5.59</i>	<i>0.77</i>

Table 1: Empirical (over 400 simulation runs) Mean Integrated Square Errors ($\times 10^4$) and *standard deviations in italic* for kernels g_j ($j = 1, \dots, 5$), unknown functions f_1 to f_3 , $n = 100$ and $n = 250$, and, for the noise level equals to $\sigma_0(g_j)/2^i$, $i = 1, \dots, 5$.